Rayleigh Wave Attenuation and Amplification Measured at Ocean-Bottom Seismometer Arrays using Helmholtz Tomography

Joshua B. Russell[1], Colleen A. Dalton[1]

[1]Department of Earth, Environmental, and Planetary Sciences, Brown University, Providence, RI, USA

Corresponding author: Joshua B. Russell (joshua_russell@brown.edu)

Key Points:

- Helmholtz tomography applied at ocean-bottom seismometer arrays recovers Rayleigh wave attenuation and site amplification at 20–150 s period

- Synthetic tests show that focusing/defocusing are successfully accounted for, including near the coastline where strong multipathing occurs

- Strong site amplification observed at the Juan de Fuca ridge may be used to improve models of crust and shallow mantle

15 **Abstract**

16 Shear attenuation provides insights into the physical and chemical state of the upper mantle. Yet,
17 observations of attenuation are infrequent in the oceans, despite recent proliferation of arrays of
18 ocean-bottom seismometers (OBS). Studies of attenuation in marine environments must
19 overcome unique challenges associated with strong oceanographic noise at the seafloor and data
20 loss during OBS recovery in addition to untangling the competing influences of elastic focusing,
21 local site amplification, and anelastic attenuation on surface-wave amplitudes. We apply
22 Helmholtz tomography to OBS data to simultaneously resolve array-averaged Rayleigh wave
23 attenuation and maps of site amplification at periods of 20–150 s. The approach explicitly
24 accounts for elastic focusing and defocusing due to lateral velocity heterogeneity using wavefield
25 curvature. We validate the approach using realistic wavefield simulations at the NoMelt
26 Experiment and Juan de Fuca (JdF) plate, which represent endmember open-ocean and coastline-
27 adjacent environments, respectively. Focusing corrections are successfully recovered at both
28 OBS arrays, including at periods < 35 s at JdF where coastline effects result in strong
29 multipathing. When applied to real data, our observations of Rayleigh wave attenuation at
30 NoMelt and JdF revise previous estimates. At NoMelt, we observe a low attenuation lithospheric
31 layer (Q_μ>1500) overlying a highly attenuating asthenospheric layer (Q_μ~50–70). At JdF, we
32 find a broad peak in attenuation (Q_μ~50–60) centered at a depth of 100–130 km. We also report
33 strong local site amplification at the JdF Ridge (>10% at 31 s period), which can be used to
34 refine models of crust and shallow mantle structure.

35 **Plain Language Summary**

36 Seismic tomography provides a tool for probing regions deep within the Earth that are otherwise
37 inaccessible. The degree to which seismic waves lose energy as they travel (seismic attenuation)
38 provides information about temperature and melt in Earth's interior. However, seismic
39 attenuation is notoriously difficult to measure due to complicating effects on wave amplitudes
40 from focusing and amplification of the waves as they travel through the heterogeneous Earth.
41 Here we introduce a tool that utilizes both amplitude and travel-time information observed across
42 arrays of seismometers to account for these competing effects and accurately quantify seismic
43 attenuation. We validate the approach using realistic simulations and apply it to real datasets at
44 young (~3 Myr) and older (~70 Myr) locations in the Pacific Ocean. Our observations revise
45 previous estimates of attenuation at the two locations, revealing high attenuation that extends
46 deeper beneath the Juan de Fuca ridge than previously thought and high attenuation in the
47 asthenosphere beneath the typical oceanic plate. These observations have important implications
48 for our understanding of mantle temperature and melt content beneath the oceans.

49 **1 Introduction**

50　　　　Shear attenuation of the upper mantle is a key parameter for quantifying the physical and
51 chemical state of the asthenosphere. As attenuation and shear velocity respond differently to
52 variations in temperature, melt fraction, grain size, and volatile content (Faul & Jackson, 2005;
53 Jackson & Faul, 2010; McCarthy et al., 2011; McCarthy & Takei, 2011; Yamauchi & Takei,
54 2016), jointly interpreting these two observables offers unprecedented constraints on upper
55 mantle properties (Dalton & Faul, 2010; Debayle et al., 2020; Havlin et al., 2021; Priestley &
56 McKenzie, 2013; Richards et al., 2020). In contrast to shear velocity, which is routinely
57 constrained at local and regional scales, our understanding of upper-mantle attenuation is largely
58 limited to global models derived from Rayleigh wave observations (e.g., Adenis et al., 2017b,

59 2017a; Dalton et al., 2008; Karaoğlu & Romanowicz, 2018). This is especially true of the ocean
60 basins where station coverage is sparse compared to the continents. In global models, shear
61 attenuation beneath the ocean basins is primarily constrained by basin-traversing Rayleigh waves
62 with long ray paths that tend to smear structure both laterally and vertically.

63   A primary challenge for all studies of Rayleigh wave attenuation is isolating the signal of
64 attenuation in amplitude measurements from other effects, including source excitation,
65 focusing/defocusing, and local site amplification. While progress has been made at longer
66 periods at the global scale (e.g., Dalton & Ekström, 2006), the ability to robustly account for
67 these effects at higher frequencies at regional and local scales is still a topic of active
68 development (e.g., Forsyth & Li, 2005; F. C. Lin et al., 2012; Yang & Forsyth, 2006). Improving
69 resolution of upper-mantle shear attenuation requires innovative seismic techniques that resolve
70 regional-scale Rayleigh wave attenuation while accurately accounting for these additional factors
71 that complicate wave amplitudes.

72   New surface-wave imaging techniques have been developed in recent years owing to an
73 abundance of high-quality broadband seismic datasets with dense and uniform station coverage,
74 such as the USArray. These techniques make use of the spatial gradients of Rayleigh wave
75 amplitude and phase to extract structural information from the wavefield. Perhaps the most
76 widely used to date is Helmholtz tomography, which yields regional-scale maps of phase
77 velocity while accounting for finite-frequency effects (Jin & Gaherty, 2015; F.-C. Lin &
78 Ritzwoller, 2011). The approach is attractive due to its simplicity compared to alternatives such
79 as wave gradiometry (Langston, 2007a, 2007c, 2007b; Y. Liu & Holt, 2015) and requires fewer
80 physical assumptions about the wavefield compared to simpler techniques such as the two-plane
81 wave (TPW) method, which approximates the wavefield as the superposition of two plane waves
82 with varying phase and amplitude (Forsyth & Li, 2005). Furthermore, the openly available
83 Automated Surface-Wave Measurement System (ASWMS) software package has made
84 Helmholtz tomography widely accessible to the seismology community (Jin & Gaherty, 2015).
85 F. C. Lin et al. (2012) recently developed an extension of Helmholtz tomography for estimating
86 Rayleigh wave attenuation and site amplification, which has been applied to USArray data (Bao
87 et al., 2016; Bowden et al., 2017; F. C. Lin et al., 2012). However, it is not yet clear how
88 effectively the technique can be applied at smaller scale arrays with often less optimal array
89 geometries.

90   Despite recent methodological advances on land, seismic imaging in marine
91 environments lags due to challenges associated with the relatively noisy seafloor environment
92 and often sparse station coverage compared to terrestrial seismic deployments. This is true
93 especially for studies of Rayleigh wave attenuation across arrays of ocean-bottom seismometers
94 (OBS), where only a handful of observations have been made to date (e.g., Ma et al., 2020; Ruan
95 et al., 2018; Saikia et al., 2021; Yang & Forsyth, 2006). To our knowledge, all existing regional
96 Rayleigh wave attenuation observations made in the oceans were measured using the TPW
97 method. While TPW provides a simple approach for measuring 1-D Rayleigh wave attenuation
98 in the presence of weak or moderate multipathing, it may suffer in complex regions such as near
99 the coastlines, where the wavefield may not be well approximated by two interfering plane
100 waves. Furthermore, we are unaware of any previous reports of Rayleigh wave site amplification
101 in the oceans, despite having sensitivity to elastic structure that complements that of phase
102 velocity (F. C. Lin et al., 2012; Schardong et al., 2019). Helmholtz tomography offers a
103 promising approach that can simultaneously constrain attenuation and site amplification while

104 accurately accounting for wavefield focusing/defocusing. However, it is unclear whether typical
105 OBS array geometries and earthquake distributions offer the resolution needed for the technique
106 to be successful as all previous applications have used well-behaved USArray data.

107 In this study, we show that Helmholtz tomography can be used to reliably measure array-
108 averaged Rayleigh wave attenuation and 2-D maps of site amplification in oceanic settings,
109 offering an alternative to the TPW method. We validate the approach using realistic wavefield
110 simulations through 3-D elastic structure, demonstrating its ability to account for
111 focusing/defocusing and recover attenuation and amplification. The methodology is applied at
112 two OBS arrays representing endmember locales (open ocean and coastline adjacent) with
113 apertures on the order of 500x500 km^2. Our observations revise previous estimates of Rayleigh
114 wave attenuation at the two locations and provide perhaps the first measurements of site
115 amplification in an oceanic setting. We implement the approach as an add-on to the ASWMS
116 software, offering a new tool for estimating Rayleigh wave attenuation and amplification across
117 regional-scale arrays that has been validated by realistic synthetic seismograms.

2 Data and Measurements

119 Broadband waveform data are utilized from the NoMelt Experiment and the Juan de Fuca
120 (JdF) portion of the Cascadia Initiative, located in the central and eastern Pacific, respectively
121 (Figure 1). The NoMelt experiment was positioned approximately 1200 km southeast of Hawaii
122 on unperturbed, ~70 Ma seafloor far from hotspot, ridge, or subduction influences (P.-Y. P. Lin
123 et al., 2016; Ma et al., 2020; Mark et al., 2019; Russell et al., 2019). The experiment consisted of
124 a reflection/refraction survey (Mark et al., 2019), a magnetotelluric deployment (Sarafian et al.,
125 2015), and a broadband OBS deployment from December 2012 to December 2013 (P.-Y. P. Lin
126 et al., 2016; Ma et al., 2020; Mark et al., 2021; Russell et al., 2019). Here, we make use of the 16
127 broadband OBS with an array aperture of 400x600 km^2. Station depths range from 4889–5331 m
128 below the sea surface.

129 The Cascadia Initiative was an amphibious experiment consisting of a multi-year
130 broadband OBS deployment spanning the JdF and Gorda plates (Bell et al., 2016; Byrnes et al.,
131 2017; Eilon & Forsyth, 2020; Hawley et al., 2016; Janiszewski et al., 2019; Ruan et al., 2018).
132 We use data from the year 1 (23 stations; November 2011—May 2012) and year 3 (27 stations;
133 August 2013—May 2014) deployments co-located on the JdF plate seaward of the trench. Here,
134 water depth ranges from 2544 m to 2940 m. We avoid stations in shallow water near the
135 continental shelf due to noisier conditions and crust and mantle structure that is complicated by
136 subduction processes (Janiszewski et al., 2019). While the majority of the 400x400 km^2
137 deployment footprint is characterized by nascent oceanic plate (~3 Ma average seafloor age), the
138 JdF Ridge cuts NNE-SSW across the western edge of the array (Figure 1b).

139 The NoMelt and Juan de Fuca regions represent endmembers in terms of their seafloor
140 age, structural complexity, and noise environment. The NoMelt experiment exemplifies an ideal
141 OBS deployment for Rayleigh wave imaging. Its location in the center of the plate provides
142 excellent azimuthal coverage for teleseismic Rayleigh waves, and the deep (~5000 m depth)
143 open-ocean environment offers relatively quiet noise conditions. As most paths from source to
144 receiver consist of largely homogeneous oceanic material, most arriving Rayleigh waves show
145 little to no evidence of multipathing (Ma et al., 2020). In contrast, JdF represents a more
146 challenging coastal environment. The region is characterized by shallower water depths (~2700
147 m) with higher noise levels and has azimuthal gaps in teleseismic earthquakes to the south and

148 northeast. Additionally, large lateral gradients in velocity structure associated with the continent-
149 ocean transition can produce complex Rayleigh waveforms exhibiting multipathing and
150 scattering, particularly for waves traveling parallel to the coastline (Bell et al., 2016). These
151 differences between the two focus sites allow us to test the limitations of the imaging approach.
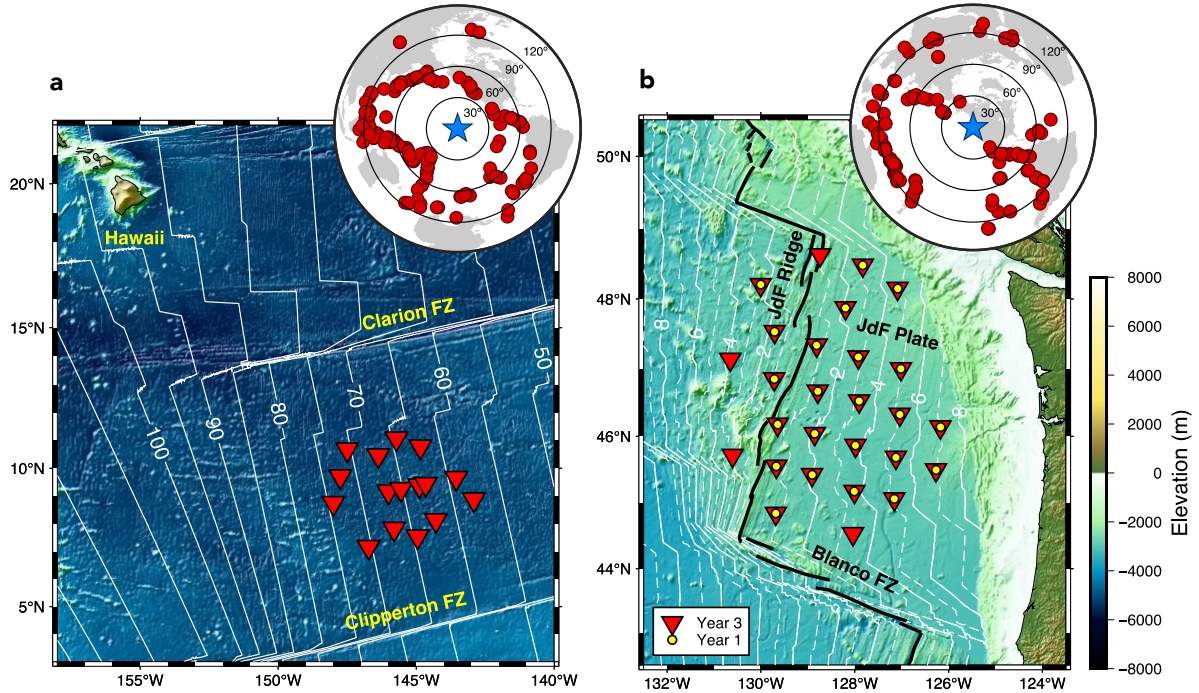

152
153 **Figure 1.** Maps of station locations for the (a) NoMelt experiment and (b) Juan de Fuca (JdF)
154 component of the Cascadia Initiative. Event locations are shown at the top right of each panel.
155 Seafloor age contours (white; labels in Myr) are from Seton et al. (2020). FZ = fracture zone

156   We retrieve four-component (3 directional and pressure-gauge) data for earthquakes in
157 the Global Centroid Moment Tensor (GCMT) catalogue (Ekström et al., 2012) with Mw > 5.5,
158 depths < 50 km, and epicentral distances ranging from 20º to 100º. Events with epicentral
159 distances > 100º are avoided as they are more likely to have complicated paths (i.e., large
160 portions that pass through continents), and Rayleigh wave phase and amplitude measurements
161 for distances > 120º can be contaminated by major arc overtones (Hariharan et al., 2020).
162 Although fundamental-mode Rayleigh wave excitation typically peaks at depths < 50 km, our
163 dataset could be expanded in the future by considering deeper (primarily vertical dip-slip)
164 earthquakes with considerable excitation below 50 km (Hariharan et al., 2022). As a rough initial
165 quality control metric, we consider only events for which the vertical component Rayleigh wave
166 appears at more than 5 stations with a signal-to-noise ratio (SNR) > 3 in the period band 20–80 s.
167 In total, these criteria yielded 191 earthquakes for the NoMelt dataset and 160 earthquakes for
168 JdF. That more events meet these criteria at NoMelt, which was deployed nearly half as long as
169 JdF, is largely a result of the lower noise levels at those stations.

170   2.1 Noise corrections

171   Vertical component OBS data is often contaminated by tilt and compliance noise.
172 Bottom-current noise typically contaminates the horizontal channels but can appear on the

173   vertical channel as tilt noise if the instrument is slightly rotated from vertical (Crawford & Webb,
174   2000). Compliance noise results from long-period infragravity waves that produce pressure
175   perturbations at the seafloor (Webb & Crawford, 1999). Both tilt and compliance noise typically
176   dominate at periods > 80 s (depending on water depth) and therefore must be removed in order to
177   make robust long-period surface-wave measurements. Tilt and compliance noise are removed
178   from each vertical channel seismogram by applying the Automated Tilt and Compliance
179   Removal (ATaCR) software package (Janiszewski et al., 2019). This tool employs the
180   methodology developed by Crawford & Webb (2000) to estimate and remove coherent signals
181   between the vertical and two horizontal channels and the vertical and pressure channel.

182   2.2 Phase and amplitude measurements

183   Rayleigh wave phase and amplitude are measured using the ASWMS software package,
184   described in detail by Jin & Gaherty (2015). The tool employs a cross-correlation based
185   approach to measure frequency-dependent interstation phase and group delay times and single-
186   station amplitudes, and here we summarize the procedure. Each waveform is prefiltered using a
187   second-order Butterworth filter with corner frequencies at ±25% of the maximum and minimum
188   frequencies of interest. After prefiltering and windowing each seismogram around the Rayleigh
189   wave arrival using an automated procedure, cross-correlations are calculated between all station
190   pairs within each array. Cross-correlations with a correlation coefficient <0.65 are discarded. The
191   remaining cross-correlation functions are narrow band filtered, and a five parameter Gaussian
192   wavelet is fit at each frequency, yielding frequency-dependent interstation phase and group
193   travel times, $\delta\tau_{ij}$ and $\delta\tau_{ij}^{g}$, for each station pair (i, j). Frequency-dependent amplitude
194   measurements, A_i, are obtained at a single station by applying the same Gaussian wavelet fitting
195   procedure to the autocorrelation function and taking the square root of the wavelet amplitude.
196   This procedure is implemented in two overlapping frequency bands from 20–84 s and 73–150 s,
197   resulting in measurements made at 15 periods between 20 and 150 s.

198   **3 Methods**

199   This section outlines the main equations governing our approach for estimating Rayleigh
200   wave attenuation and site amplification using observations of phase and amplitude. The
201   methodology is implemented as an add-on to the ASWMS software (see Open Research
202   statement).

203   3.1 Helmholtz tomography

204   In its most common application, Helmholtz tomography (sometimes referred to as
205   wavefront tracking) offers a method to solve for Rayleigh wave phase velocity maps, $c(x, y)$,
206   where x is longitude and y is latitude, from observations of phase delay, $\tau(x, y)$, and amplitude,
207    $A(x, y)$ (Jin & Gaherty, 2015; F.-C. Lin & Ritzwoller, 2011). More recently, this technique has
208   been extended for measuring Rayleigh wave attenuation and amplification at the USArray (Bao
209   et al., 2016; F. C. Lin et al., 2012). Here, we briefly outline the main equations that govern the
210   approach, relying heavily on the original derivation by F. C. Lin et al. (2012).

211   Consider a 2-D surface wave potential of the form $\chi(x, y, t) =$
212    $A(x, y)\beta(x, y)^{-1} \exp\{i\omega(t - \tau(x, y))\}$. This surface-wave potential satisfies the 2-D

213 homogeneous damped wave equation (Tromp & Dahlen, 1992) and balancing the real and
214 imaginary parts yields the following two equations, respectively:

215

$$\frac{1}{c(x,y)^2} = \frac{1}{c'(x,y)^2} - \frac{\nabla^2(A(x,y)/\beta(x,y))}{\omega^2(A(x,y)/\beta(x,y))}$$

(1)

216

$$\underbrace{2\nabla\tau(x,y) \cdot \frac{\nabla\beta(x,y)}{\beta(x,y)}}_{\substack{\text{local amplification} \\ \text{gradient}}} - \underbrace{\frac{2\alpha(x,y)}{c(x,y)}}_{\substack{\text{anelastic} \\ \text{attenuation} \\ \text{term}}} = \overbrace{\underbrace{2\nabla\tau(x,y) \cdot \frac{\nabla A(x,y)}{A(x,y)}}_{\substack{\text{apparent amplitude} \\ \text{decay}}} + \underbrace{\nabla^2\tau(x,y)}_{\substack{\text{focusing} \\ \text{correction}}}}^{\text{corrected amplitude decay}}$$

(2)

217

218 where ω is angular frequency, $c'(x,y) = |\nabla\tau(x,y)|^{-1}$ is apparent phase velocity, $c(x,y)$ is
219 structural phase velocity, $\alpha(x,y)$ is the anelastic attenuation coefficient, and $\beta(x,y)$ is relative
220 local site amplification of the surface-wave potential. For brevity, we drop the dependence on
221 position (x,y) for the remainder of this manuscript. The anelastic attenuation parameter α is
222 related to Rayleigh wave attenuation, Q^{-1}, by $\alpha = \omega/2CQ$, where C is group velocity. Because
223 attenuation varies more strongly than group velocity, spatial variations in α should mostly reflect
224 variations in Q^{-1}. Local amplification, β, is a relative measure of local amplitude and is sensitive
225 to depth-dependent elastic structure at the receiver. Values of $\beta > 1$ indicate wave amplification
226 and values of $\beta < 1$ correspond to wave deamplification. As pointed out by Bowden et al. (2017),
227 β represents amplification of the surface-wave potential, which is not directly observable, and
228 therefore it is not strictly equivalent to site amplification determined from more direct methods
229 derived from amplitude ratios (e.g., Eddy & Ekström, 2014, 2020). The two quantities can be
230 related via phase velocity through the expression $A_R/A_{R,0} = \beta\sqrt{c/c_0}$, where A_R is the Rayleigh
231 wave amplification observed at a receiver of interest compared to a reference location $A_{R,0}$, and
232 c/c_0 is the fractional difference in phase velocity relative to the value at the reference location.

233 Equation (1) with $\beta = 1$ is commonly referred to as the Helmholtz equation and can be
234 used to solve for the structural phase velocity, c, given observations of τ and A (F.-C. Lin &
235 Ritzwoller, 2011). The second term on the right-hand side that includes the Laplacian of the
236 amplitude field normalized by ω^2 accounts for finite-frequency effects. In the high-frequency
237 limit (i.e., ray theory), this term becomes negligible, and equation (1) reduces to the Eikonal
238 equation (F.-C. Lin et al., 2009). For the purposes of this study, we assume $\beta = 1$ when solving
239 equation (1) but not when solving equation (2).

240 Equation (2) is sometimes referred to as the transport equation and connects unknown
241 quantities β and α on the left-hand side to spatial derivatives of measurable quantities τ and A on
242 the right-hand side. Following the nomenclature of F. C. Lin et al. (2012), the first term on the
243 right-hand side of equation (2) is the "apparent amplitude decay" in the direction of wave
244 propagation and the second term consisting of the Laplacian of travel time is the "focusing
245 correction". The entire right-hand side is referred to as the "corrected amplitude decay". On the
246 left-hand side, we refer to the first and second terms as the "local amplification gradient" and
247 "anelastic attenuation term", respectively.

248 Measured surface-wave amplitudes $A(\omega)$ include contributions from earthquake source
249 excitation A_S, local receiver effects A_R, elastic focusing A_F, and amplitude decay due to anelastic
250 attenuation along the ray path A_Q (Dalton & Ekström, 2006):

251

$$A(\omega) = A_S(\omega)\, A_R(\omega)\, A_F(\omega)\, A_Q(\omega) \qquad (3)$$

252

253 Isolating the contribution from anelastic attenuation is the primary goal of all attenuation
254 tomography, and in Section 3.2 we describe how our methodology is able to do so. The receiver
255 term, A_R, includes contributions from instrument response, tilt and compliance noise, and local
256 site amplification. The former two contributions are removed prior to making measurements by
257 deconvolving instrument response to displacement and subtracting tilt and compliance noise as
258 described in Section 2.1, respectively. On the other hand, local site amplification, β, that results
259 from energy amplification or deamplification due to elastic structure beneath the receiver, is
260 solved for simultaneously alongside anelastic attenuation. Any imperfections in the instrument
261 response and/or tilt and compliance removal steps at individual stations will map into site
262 amplification and should not greatly affect attenuation measurements.

263 Elastic focusing and defocusing, A_F, describes horizontal refraction of the wavefield that
264 occurs due to lateral gradients in wavespeed in the Earth. Focusing and defocusing is especially
265 prevalent near the coastlines, where large velocity gradients often exist (e.g., Russell & Gaherty,
266 2021). This behavior is reflected in the wavefield curvature and is accounted for by the focusing
267 correction term, $\nabla^2\tau$, in equation (2). However, the $\nabla^2\tau$ term also includes simple geometrical
268 spreading of the 2-D surface-wave wavefield, which results in defocusing and focusing at
269 epicentral distances <90º and >90º, respectively, and can be expressed analytically as $\nabla^2\tau_{GS} =$
270 $(cR\tan X)^{-1}$, where X is epicentral distance in degrees and R is Earth's radius, and the subscript
271 "GS" stands for geometrical spreading (see Supplementary Information; Text S1; Figure S2).
272 Therefore, focusing due only to structural heterogeneity along the ray path is given by

273

$$\nabla^2\tilde{\tau} = \nabla^2\tau - \nabla^2\tau_{GS} \qquad (4)$$

274

275 We refer to this quantity as the structural focusing correction term. As it is independent of
276 epicentral distance, this term is informative when considering the overall focusing behavior
277 based on data from many earthquakes (see Section 5.1).

278

279 The source term, A_S, includes azimuthal variations in Rayleigh wave amplitude
280 associated with the radiation pattern. Surface waves emitted near nodes in the radiation pattern
281 should be avoided as excitation is both weak and varies rapidly with azimuth. However, this bias
282 has only a small effect on our amplitude dataset for three main reasons. First, the governing
283 equation (2) depends on the amplitude variation in the direction of propagation (i.e., the dot
284 product on the right-hand side), whereas the radiation pattern introduces amplitude variations
285 perpendicular to the propagation direction. Second, the requirement that SNR > 3 as mentioned
286 in Section 2 implicitly removes nodal events from our dataset. Third, the relatively small

287 ~500x500 km^2 array footprint corresponds to only a small azimuthal range for a given
288 teleseismic earthquake. Indeed, even at the larger USArray, Bao et al. (2016) found this bias to
289 be small compared to other sources of error. We tested restricting our dataset to source excitation
290 ratios >60% of the maximum to explicitly avoid nodes, but we observed no significant
291 improvement (see Supplementary Figure S3), and a large portion of the dataset was lost (~50–
292 60% of events), degrading azimuthal coverage. For these reasons, we do not explicitly account
293 for source excitation.

294   3.2 Solving for attenuation and site amplification

295   The local amplification gradient (first term in equation (2)) depends on propagation
296 azimuth via the dot product with $\nabla\tau$, while the attenuation term containing α is independent of
297 azimuth. To solve for the attenuation coefficient α and amplification β, we follow the curve-
298 fitting approach of Bao et al. (2016). The local amplification gradient term can be expanded as

299

$$2|\nabla\tau|\left|\frac{\nabla\beta}{\beta}\right|\cos(\theta - \psi_\beta) = 2|\nabla\tau|\left(\partial_x(\ln\beta)\sin\theta + \partial_y(\ln\beta)\cos\theta\right) \tag{5}$$

300

301 where θ is the azimuth of wave propagation determined by $\theta = \tan^{-1}(\partial_x\tau/\partial_y\tau)$, and shorthand
302 is used for spatial derivatives: $\partial_x = \partial/\partial x$, $\partial_y = \partial/\partial y$. The magnitude and azimuth of the local
303 amplification gradient are given by $\left|\frac{\nabla\beta}{\beta}\right| = \sqrt{\partial_x(\ln\beta)^2 + \partial_y(\ln\beta)^2}$ and $\psi_\beta = \tan^{-1}\left(\partial_x(\ln\beta)/\right.$
304 $\left.\partial_y(\ln\beta)\right)$, respectively. Substituting equation (5) into equation (2), replacing $|\nabla\tau|$ with $1/c'$, and
305 multiplying both sides by $-c/2$ yields the simplified expression:

306

$$\alpha - \gamma\left(\partial_x(\ln\beta)\sin\theta + \partial_y(\ln\beta)\cos\theta\right) = \underbrace{-\frac{c}{2}\left(2\nabla\tau\cdot\frac{\nabla A}{A} + \nabla^2\tau\right)}_{\text{apparent attenuation}} \tag{6}$$

307

308 where c is estimated from equation (1) using ASWMS (Jin & Gaherty, 2015) and $\gamma = c/c'$
309 describes biases due to finite-frequency effects. When finite-frequency effects are small (i.e.,
310 $\nabla^2 A/\omega^2 A \approx 0$), structural phase velocity and apparent phase velocity are similar in value and
311 $\gamma \approx 1$, as assumed by previous authors (Bao et al., 2016; Bowden et al., 2017; F. C. Lin et al.,
312 2012). However, we find that γ-1 can exceed $\pm10\%$ (i.e., $\gamma < 0.9$ or $\gamma > 1.1$), particularly at the
313 longest periods (>130 s). The right-hand side of equation (6) is referred to as the "apparent
314 attenuation" and is a measured quantity for each earthquake in our dataset. The left-hand side of
315 equation (6) contains the desired structural parameters—attenuation and site amplification—
316 common to all events. To solve for attenuation and amplification, the observations on the right-
317 hand side are fit to a sinusoidal curve as a function of azimuth; the static offset of the sinusoid
318 relates to α, while the amplitude and phase of the azimuthally varying part are related to β
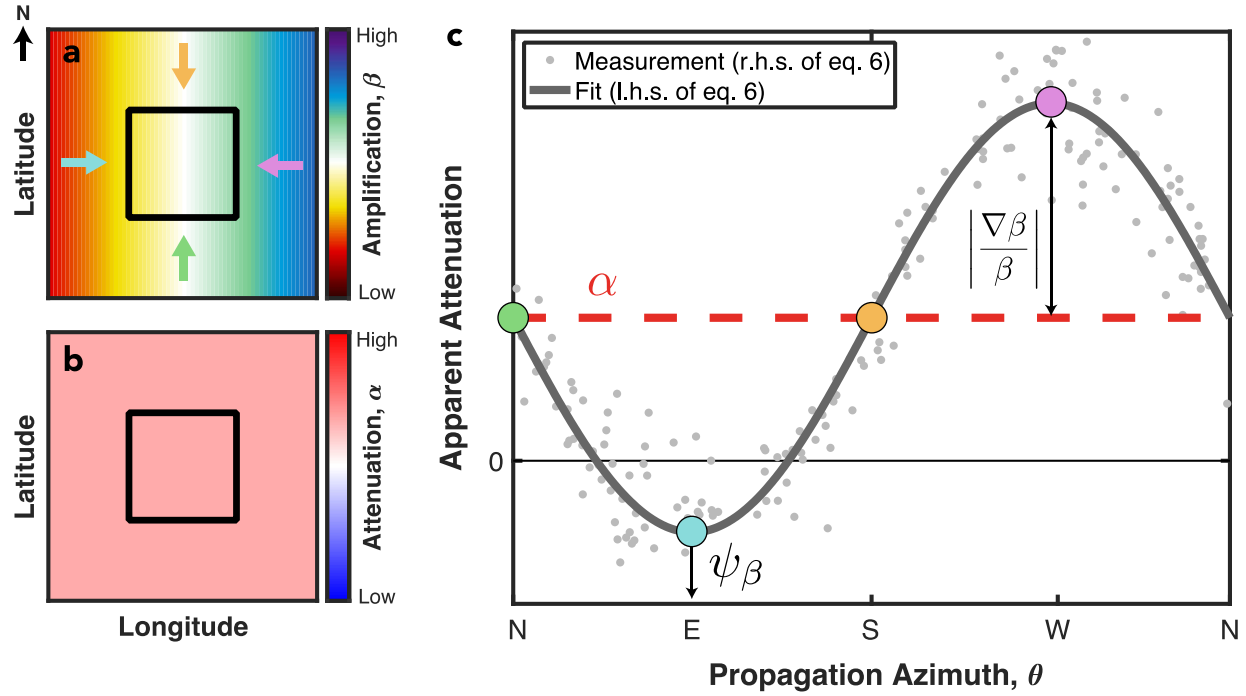319 (Figure 2).

Figure 2. Schematic illustration of equation 6 for constraining amplification gradient and attenuation. (a) Map of amplification smoothly increasing to the east. Colored arrows show direction of wave propagation for four scenarios indicated by circles in c). The black box represents the region of analysis. (b) Idealized 1-D attenuation map. (c) Apparent attenuation as a function of azimuth that would be measured within the black boxed region using data from many different earthquakes. Each gray dot represents one measurement (with noise, for illustration) for a single earthquake and pixel in the black boxed region. The dark gray curve shows the sinusoidal fit from the left-hand side of equation 6, and the red dashed line indicates the corresponding attenuation estimate. The large colored circles correspond to each of the cardinal directions of propagation in a).

Maps of apparent attenuation are estimated on an evenly spaced grid with pixel dimensions 0.5°×0.5°. We use γ as an additional quality control parameter, removing pixels for a given event in which $\gamma < 0.9$ or $\gamma > 1.1$ in order to ensure that only the highest quality measurements are considered. For our dataset, this threshold is exceeded only at the very longest periods for a small fraction of pixels. For example, only ~8% of pixels are discarded at 130 s period and ~18% are removed at 150 s period. We also discard pixels for a given event with a measured propagation azimuth $> 10°$ from the great-circle path.

Least-squares inversion of equation (6) yields log amplification gradients, $\partial_x(\ln \beta)$ and $\partial_y(\ln \beta)$, and attenuation coefficient, α, at a given pixel. In practice, it is rare that a single pixel provides a sufficient number of measurements to robustly resolve attenuation and site amplification, and therefore, data from nearby pixels can be grouped together to increase the number of measurements available for inversion. This results in maps that are inherently smoothed by a length proportional to the grouped region. In other words, there is a tradeoff between map robustness (grouping more pixels) and sharpness of lateral variations (grouping fewer pixels). To ensure smooth, well constrained maps, we adopt a binning approach whereby data within 1.5° of a central pixel are gathered and binned within 20° non-overlapping azimuthal

347   bins. The inverse standard deviation of measurements within each azimuthal bin is used to
348   weight the least squares inversion. This procedure is repeated across the study region, producing
349   smoothed 2-D maps of $\partial_x(\ln\beta)$, $\partial_y(\ln\beta)$, and α. In practice, we do not interpret 2-D variations
350   in attenuation due to the small array geometries and uneven azimuthal coverage, and instead, we
351   solve for an array-averaged α by gathering measurements from all pixels within the array and
352   performing a single inversion.

353   The resulting maps of $\partial_x(\ln\beta)$ and $\partial_y(\ln\beta)$ are used to invert for $\ln\beta$ via the centered 2-
354   D finite-difference formula. The approximate derivatives of log amplification at pixel (x_0, y_0)
355   are given by

356

$$\partial_x(\ln\beta)\big|_{(x_0,y_0)} = \frac{\ln\beta_{(x_0+1,y_0)} - \ln\beta_{(x_0-1,y_0)}}{2\Delta_x} \tag{7}$$

$$\partial_y(\ln\beta)\big|_{(x_0,y_0)} = \frac{\ln\beta_{(x_0,y_0+1)} - \ln\beta_{(x_0,y_0-1)}}{2\Delta_y} \tag{8}$$

357

358   where Δ_x and Δ_y is the grid spacing in the x and y directions. The least-squares inversion is
359   unable to recover absolute amplification, and instead, we solve for the relative amplification by
360   requiring that the mean of all $(\ln\beta)$ values within the study region is zero. This is equivalent to
361   ensuring that the average β is equal to one. Additional smoothing is imposed on $\ln\beta$ maps by
362   requiring small second spatial derivatives, $\nabla^2(\ln\beta) \approx 0$.

363   3.3 Constructing the gradient and Laplacian fields

364   The gradient and Laplacian fields of amplitude and phase travel time are required to
365   construct the apparent attenuation term and solve equation (6) for the attenuation coefficient and
366   local site amplification. One approach for estimating these fields for a given earthquake is to first
367   fit smooth surfaces to absolute phase and amplitude measurements recorded at individual stations
368   and then calculate the spatial gradients of these surfaces using finite-difference operators
369   (Chevrot & Lehujeur, 2022; F.-C. Lin et al., 2009; F.-C. Lin & Ritzwoller, 2011). Removal of
370   outliers is an important step prior to the surface fitting procedure to avoid anomalies in the
371   surface that can amplify upon differentiation. This point is especially crucial for the Laplacian,
372   which requires twice differentiation. Various fitting and regularization approaches have been
373   used such as minimum curvature surface fitting (Bao et al., 2016; F.-C. Lin et al., 2009; F.-C.
374   Lin & Ritzwoller, 2011), smoothing splines, and splines in tension (Chevrot & Lehujeur, 2022).
375   Each approach aims to regularize the interpolation procedure such that gradients are well
376   behaved. While minimum curvature smoothing may be acceptable for Eikonal tomography
377   (Chevrot & Lehujeur, 2022), this form of regularization tends to suppress the Laplacian fields
378   required for Helmholtz tomography, limiting one's ability to account for finite-frequency ($\nabla^2 A$)
379   and focusing/defocusing ($\nabla^2\tau$) effects.

380   We adopt an alternative approach for dealing with these challenges; our main philosophy
381   is to avoid applying direct numerical differentiation when possible. We adopt the ray
382   tomography method of Jin & Gaherty (2015), which uses the many interstation travel-time

383 measurements that were determined by cross-correlation to construct the phase slowness vector
384 field, $\nabla\tau$, directly. Below, we show how this can also be extended to the amplitude field to solve
385 for $\nabla A/A$. This approach is attractive for several reasons. First, it does not require fitting a
386 surface to single-station observations, but instead makes use of many more interstation
387 observations derived from cross-correlations and therefore should be less susceptible to noise
388 from any individual measurement. Second, the gradient field is solved for directly meaning that
389 its character (smoothness, curvature) can be easily controlled via constraint equations within the
390 inversion. Third, only one derivative is needed to calculate the Laplacian field, versus two when
391 surface-fitting is applied to single-station travel-time or amplitude measurements. Finally, formal
392 uncertainties from the inversion procedure are propagated through each step to ensure the best
393 quality measurements are being fit in equation (6) (see Supplementary Text S1 for error
394 propagation equations). We find that this ray-tomography approach more reliably recovers input
395 synthetic attenuation values compared to the surface fitting procedure in some cases (Figure S5).

396   The differential phase travel time between two stations i and j, $\delta\tau_{ij}$, is expressed as the
397 path integral of the travel-time gradient (or phase slowness) along the great-circle path
398 connecting the stations. In practice, this equation is discretized, and we solve separately for the x
399 and y components of the travel-time gradient:

400

$$\delta\tau_{ij} = \int_i^j \nabla\tau \cdot dr \approx \sum_{k=i}^{j} \partial_x\tau_k \cdot dx_k + \partial_y\tau_k \cdot dy_k \tag{9}$$

401

402 where dx_k is the path length through the kth cell projected onto the x-direction with an
403 equivalent definition for dy_k. After solving for the x and y components of the travel-time
404 gradient, apparent phase velocity maps are calculated from $c' = [(\partial_x\tau)^2 + (\partial_y\tau)^2]^{-1/2}$, and the
405 focusing corrections are given by $\nabla^2\tau = \partial_x(\partial_x\tau) + \partial_y(\partial_y\tau)$. We perform an analogous
406 inversion of group travel-times, $\delta\tau_{ij}^g$, for maps of group velocity C, allowing for the estimation
407 of Rayleigh wave attenuation via $Q^{-1} = 2C\alpha/\omega$.

408   The inverse problem for the x and y components of the gradient field is solved using a
409 least-squares approach with a second derivative smoothing (i.e., minimum curvature) constraint
410 (Jin & Gaherty, 2015). The smoothing operator is rotated to the local radial and transverse
411 directions at each grid cell (assuming great-circle propagation from the earthquake) and a
412 solution is found that minimizes the following penalty function:

413

$$E = \sum \left| \delta\tau_{ij} - \int_i^j \nabla\tau \cdot dr \right|^2 + \frac{\varepsilon\lambda}{\Delta}\sum\{|\nabla^2(\partial_R\tau)|^2 + |\nabla^2(\partial_T\tau)|^2\} \tag{10}$$

414

415 where $\partial_R\tau$ and $\partial_T\tau$ are the phase slowness parallel and perpendicular to the great-circle path,
416 respectively. The first sum is over all inter-station travel times, and the second sum is over all
417 grid cells. To impose frequency-dependent smoothing, we weight the smoothing constraint by

418 the ratio of approximate wavelength-to-grid spacing, λ/Δ. The global smoothing parameter, ε, is
419 used to balance the relative importance of data fit and model roughness, and we choose a
420 moderate value of 0.1. For our chosen grid spacing of 0.5°×0.5°, this results in overall smoothing
421 weights that range from 0.14 at a period of 20s to 1.1 at 150 s.

422   Because we solve for the gradient field directly, the second derivative smoothing
423 constraint in equation (10) is equivalent to minimizing the third spatial derivative of travel time,
424 $\nabla^3\tau$. This requires that the Laplacian field of travel time smoothly varies. While this may limit
425 our ability to resolve sharp gradients in the focusing term, $\nabla^2\tau$, it provides a robust solution
426 given the finite set of unevenly distributed observations. We choose not to apply a first derivative
427 smoothing constraint in the inversion as this would enforce propagation along a great-circle arc,
428 resulting in a focusing correction term that perfectly captures the effects of geometrical
429 spreading, $\nabla^2\tau_{GS}$, but does not account for elastic focusing and defocusing due to lateral velocity
430 gradients.

431   We use an analogous approach to solve for the normalized amplitude gradient field $\nabla A/A$
432 found in equation (6). Because our amplitude measurements are single-station values, we first
433 form the log amplitude difference between a pair of stations, $\delta\ln A_{ij} = \ln A_i - \ln A_j$, and then
434 relate it to the x and y components of the gradient field using

435

$$\delta\ln A_{ij} = \int_i^j \frac{\nabla A}{A} \cdot dr \approx \sum_{k=i}^{j} \frac{\partial_x A_k}{A_k} \cdot dx_k + \frac{\partial_y A_k}{A_k} \cdot dy_k \tag{11}$$

436

437 This expression is inverted via least squares by minimizing the penalty function analogous to
438 equation (10). With maps of $(\partial_x A/A, \partial_y A/A)$ and $(\partial_x \tau, \partial_y \tau)$ for each earthquake, we calculate
439 the amplitude gradient along the direction of propagation, $\nabla\tau \cdot \nabla A/A$, and construct the apparent
440 attenuation term (i.e., the right-hand side of equation (6)) and solve for α and β following
441 Section 3.2.

4 Synthetic Wavefield Simulations

443   Here, we describe realistic wavefield simulations that are used, in Section 5, to evaluate
444 how well attenuation and local site amplification can be recovered from typical OBS array
445 geometries. While the Helmholtz technique has been successfully applied at the USArray for
446 measuring Rayleigh wave attenuation and site amplification (Bao et al., 2016; F. C. Lin et al.,
447 2012), the technique has not yet been applied at an OBS array. In contrast to USArray's uniform
448 ~70 km station spacing, a typical OBS experiment comprises a smaller footprint with often
449 uneven station coverage due to chosen experiment geometry and/or data loss, making it more
450 difficult to accurately recover the gradient and Laplacian fields. Experiments near the continental
451 shelf, such as JdF, represent an especially challenging setting as strong focusing and
452 amplification are expected to occur due to the abrupt velocity contrast at the ocean-continent
453 transition. Additionally, conditions on the seafloor are often noisier than on land, affecting the
454 quality of travel-time and amplitude measurements. Each of these factors contributes to
455 difficulties associated with measuring intrinsic Rayleigh wave attenuation in the ocean basins.
456 To test some of these limitations and validate the approach, we apply the methodology outlined

457 in Section 3 to a realistic synthetic dataset comprising the real station and event geometry. This
458 also provides an opportunity to compare the Helmholtz approach with the two-plane-wave
459 approach (Forsyth & Li, 2005; Yang & Forsyth, 2006), which has been used to measure
460 attenuation at several OBS arrays (e.g., Ruan et al., 2018; Yang & Forsyth, 2006), in a self-
461 consistent manner.

462   We generate synthetic seismograms for all of the same events and stations used in the
463 real dataset for both the NoMelt and JdF experiments using the SPECFEM3D GLOBE software
464 (Komatitsch & Tromp, 2002b, 2002a). This includes simulations for 160 earthquakes for JdF and
465 191 at NoMelt. The 3-D elastic model used for the simulations consists of CRUST2.0 (Bassin et
466 al., 2000) overlying the mantle model S362ANI (Kustowski et al., 2008), and attenuation is
467 specified by 1-D model QL6 (Durek & Ekström, 1996). Hereafter, we refer to the full 3-D model
468 as S362ANI+CRUST2.0. The mesh is constructed such that 832 spectral elements lie along the
469 circumference of the Earth, resulting in an average spectral element width of ~48 km and a
470 minimum resolved period of ~20 s.

471   The synthetic seismograms include realistic effects on Rayleigh wave phase and
472 amplitude caused by wavefield focusing, defocusing, and scattering due to 3-D elastic
473 heterogeneity, intrinsic attenuation, local site amplification, finite-frequency effects, and
474 overtone interference. In addition to calculating seismograms at the true station locations, we
475 also sample the wavefield on an evenly spaced 0.5°x0.5° grid over a broader region centered on
476 each array (black points in Figure 3). This idealized geometry should allow us to more accurately
477 recover the true gradient and Laplacian fields, providing a benchmark for assessing how well
478 those fields are estimated using the true station geometries. The procedures used to measure
479 phase and amplitude and invert for gradient and Laplacian fields for the synthetic dataset are
480 identical to those used for the real data.

481   NoMelt and JdF represent endmember locations in terms of structural complexity. Figure
482 3 shows phase velocity maps at 31 s and 84 s period for S362ANI+CRUST2.0, which were
483 calculated by sampling 1-D profiles from the 3-D model at 1° intervals and applying MINEOS to
484 calculate Rayleigh wave dispersion. The maps have been corrected for the effect of physical
485 dispersion using a reference frequency of 1 Hz (H. Liu et al., 1976). Although the wavefield
486 simulations are performed on a fully 3-D model, these phase velocity maps are a useful
487 representation of the structure sampled by Rayleigh waves of a certain period. There is a clear
488 contrast between NoMelt and JdF, particularly at 31 s period, for which phase velocities vary by
489 more than ±2% at JdF but are typically <0.5% at NoMelt. We note that slow velocities associated
490 with the JdF Ridge (e.g., Bell et al., 2016) are absent from the coarse 3-D model. Regardless, the
491 sharp velocity contrast associated with the continent-ocean transition still allows us to test the
492 limitations of the methodology.

493   In order to avoid confusion, we define terminology to clearly distinguish between
494 quantities derived from the real dataset and those derived from the synthetic simulations.
495 Hereafter, we refer to the synthetic waveforms and measurements derived from them as
496 "synthetics" and the real observations as the "data". In addition, "measurements" are any
497 quantities estimated from Helmholtz tomography (i.e., equations 1–11) and can apply to data or
498 synthetics, and "predictions" refer to synthetic calculations of a given quantity from the
499 S362ANI+CRUST2.0 model (i.e., using MINEOS). These predictions are useful because they
500 represent the target for recovery in our synthetic tests. By comparing the synthetic measurements

501 to these predictions, we can explore limitations of the methodology related to station coverage
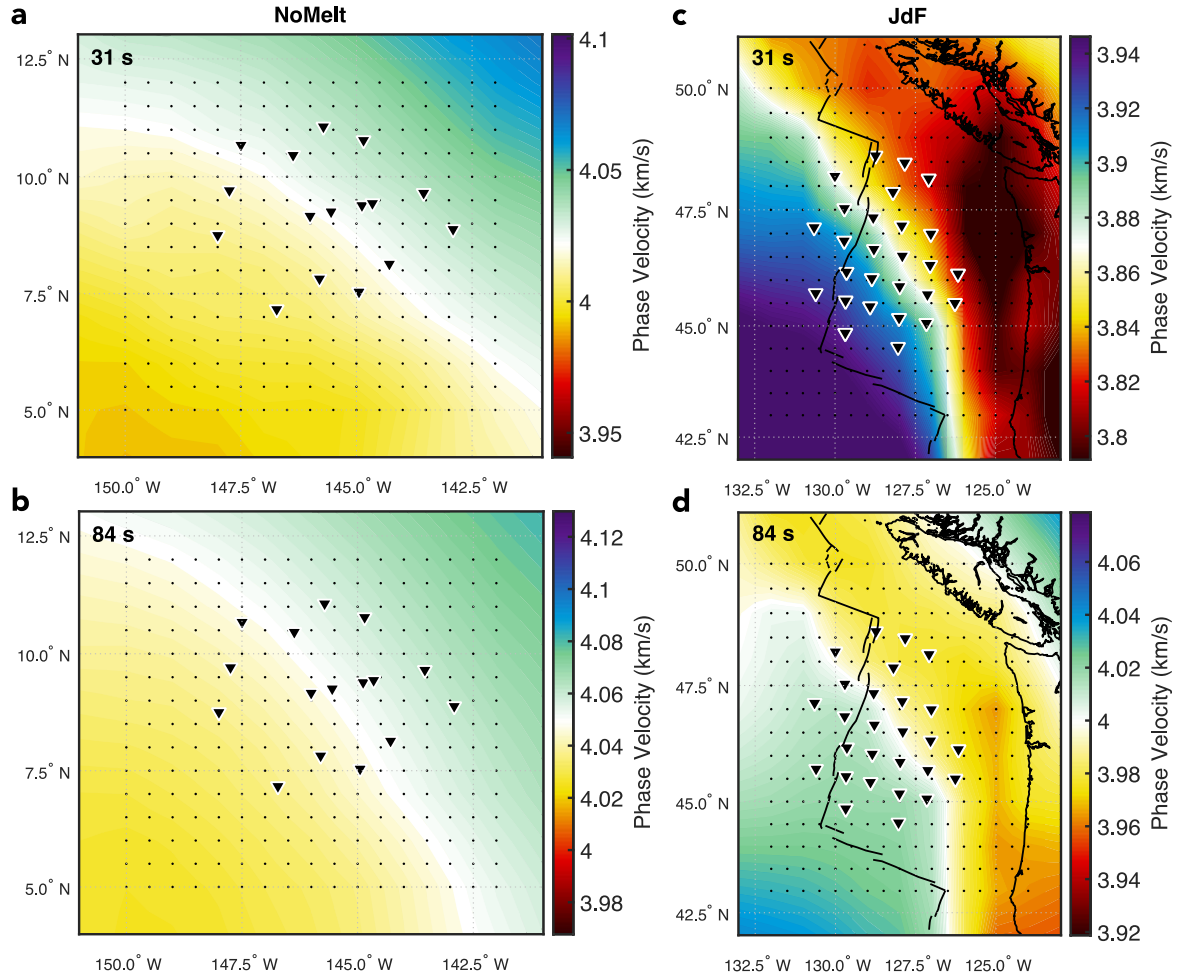502 and/or wavefield complexities.

503

Figure 3. Predicted synthetic Rayleigh wave phase velocity maps for 3-D global mantle model
505 S362ANI (Kustowski et al., 2008) combined with CRUST2.0 (Bassin et al., 2000) at (a,c) 31 s
506 and (b,d) 84 s period. Maps are predicted by sampling 1-D profiles every 1° from the 3-D model
507 and calculating dispersion using MINEOS. (left) NoMelt and (right) JdF station geometries are
508 indicated by black triangles. The finely spaced (0.5°×0.5°) black points show the locations at
509 which the SPECFEM3D GLOBE synthetic wavefield was sampled for idealized synthetic testing
510 in Figure 4a–c; this sampling interval is approximately equal to one spectral element and
511 corresponds to the grid spacing used in the ray tomographic inversion for the gradient fields.
512 Colors range from -2% to +2% about the mean velocity. Maps are corrected for physical
513 dispersion using the 1-D model QL6 (Durek & Ekström, 1996) and a reference frequency of 1
514 Hz.

5 Results

516   In the following sections, we present the results of applying equation (6) to both
517 synthetics and real data at NoMelt and JdF. Synthetics are treated identically to the data

518   throughout the analysis. First, we demonstrate the ability to faithfully recover the focusing
519   correction term ($\nabla^2 \tau$) and compare this term for the two study sites (Section 5.1). We then
520   present maps of site amplification (β) for both data and synthetic at both locations and
521   demonstrate that the measured synthetic maps match theoretical predictions (Section 5.2). Array-
522   averaged estimates of attenuation (α) are then presented for both data and synthetic, and
523   comparisons are made with the TPW technique (Section 5.3). Finally, we invert array-averaged
524   attenuation for 1-D profiles of shear attenuation (Q_μ^{-1}) at NoMelt and JdF and compare our
525   results with previous studies (Section 5.4).

526   5.1 Focusing corrections

527   Figure 4 shows example maps of apparent amplitude decay, focusing correction, and
528   corrected amplitude decay for a Mw 6.4 earthquake originating at the southern East Pacific Rise
529   and propagating north-northwest across the JdF array. The propagation direction approximately
530   parallels the coastline, representing an extreme case of focusing and defocusing that manifests as
531   strong NW-SE banding that is parallel to the direction of wave propagation in the amplitude
532   decay maps (Figure 4a,d,g). Three main observations can be made: First, the focusing effects are
533   significant and greatly impact the amplitude decay field (Figure 4a–c). Second, the true station
534   geometry is sufficient for resolving the focusing correction term and, in turn, the corrected
535   amplitude decay field (Figure 4d–f). Third, the data show a similar overall behavior to the
536   synthetic measurements, indicating that even in the noisy seafloor environment focusing effects
537   can be observed and corrected for (Figure 4g–i).

538   The amplitude decay (Figure 4a,d,g) and focusing correction terms (Figure 4b,e,h)
539   display similar patterns that are opposite in sign such that the coastline-parallel banding is
540   significantly reduced when added together to form the corrected amplitude decay map (Figure
541   4c,f,i). For this event, the sign of the strongest focusing correction is positive (blue) indicating
542   *defocusing* of the wavefield. In other words, wave amplitudes in the blue regions of Figure 4b,e,h
543   decay more strongly than dictated by intrinsic attenuation, and thus, failing to correct for
544   defocusing would result in attenuation estimates that are biased high at those pixels for this
545   event. In contrast, the region of strong amplitude decay (red) near the coastline in Figure 4a is
546   not removed by the focusing correction and therefore is likely related to site deamplification at
547   the coastline. The slightly positive regions at the edges of the corrected amplitude decay maps
548   (Figure 4f,i) are likely artifacts due to edge effects in the gradient and/or Laplacian estimates.
549   Because we consider many events from various azimuths, such edge effects do not strongly bias
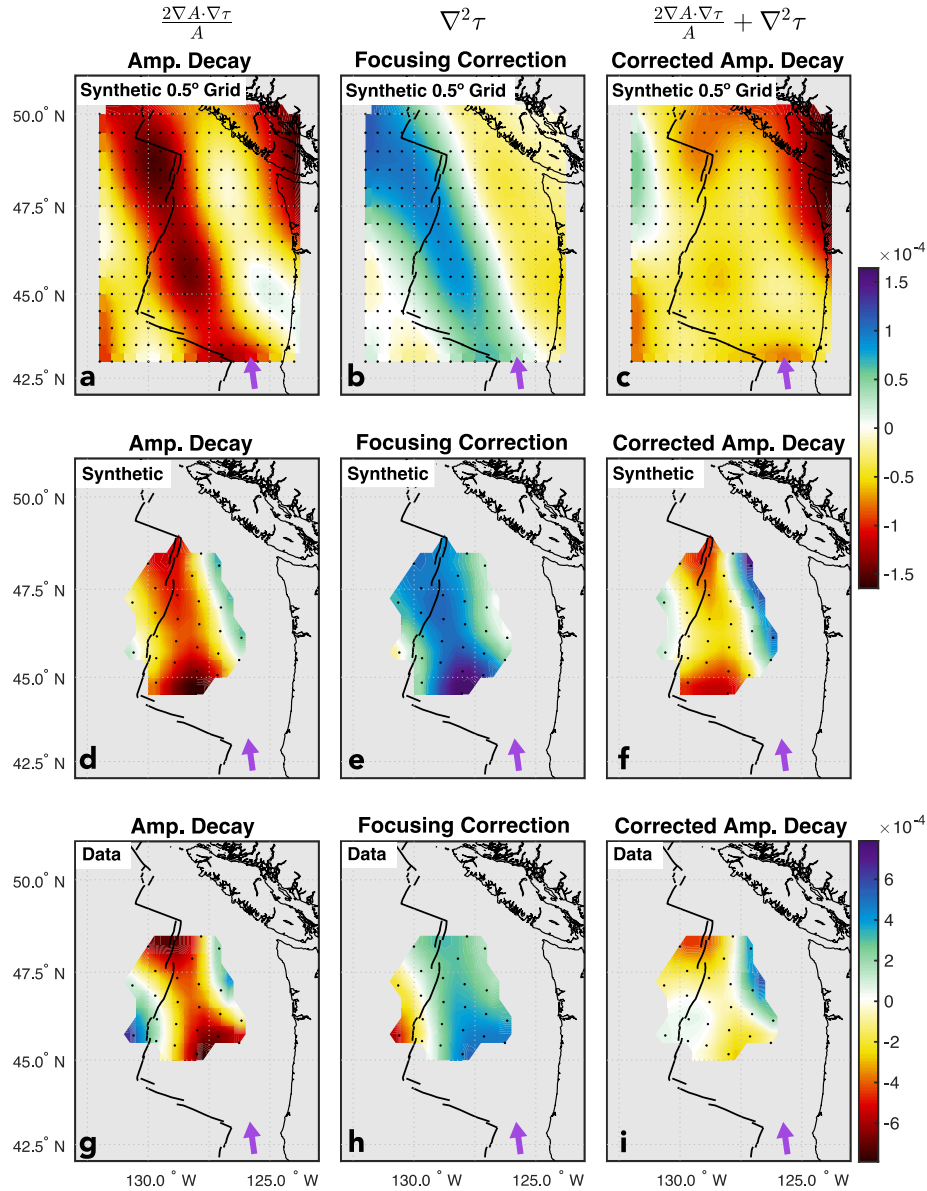550   estimates of attenuation or site amplification.

Figure 4. Demonstration of the 55 s period focusing/defocusing correction at JdF for a Mw 6.4 strike-slip earthquake that occurred at the southern East Pacific Rise on May 12, 2014 (13:58:21.5 GMT). Measured maps of (a) apparent amplitude decay, (b) focusing correction, and (c) corrected amplitude decay estimated from SPECFEM3D GLOBE synthetics for idealized station spacing of 0.5°×0.5°. Black points indicate station/sampling locations from Figure 3. The purple arrow shows the direction of wave propagation. (d–f) Same as a–c but measured from SPECFEM3D GLOBE synthetics sampled at the true OBS locations. (g–i) Same as d–f but measured from the real data. Note the larger range of values in g–i.

The resemblance between the synthetic and observed focusing corrections in Figure 4 is remarkable given the high noise levels typically associated with OBS data and suggests that the velocity structure of S362ANI+CRUST2.0 between this particular source on the East Pacific Rise and JdF receivers (see Supplementary Figure S1) resembles the true structure at 55 s period.

564   However, the maximum amplitude of the focusing corrections for the real data is larger by a
565   factor of ~5, likely due to the global model being smooth, which reduces the overall amplitude of
566   focusing and defocusing. We note that the synthetic and real gradient fields compare less
567   favorably for propagation paths that are oriented more perpendicular to the coastline (not shown)
568   as the presence of the JdF Ridge has a strong influence on the real dataset but is not well
569   resolved by the long-wavelength S362ANI+CRUST2.0 structure.

570   We further explore the focusing corrections by investigating their distribution for all
571   events in our catalogue at both NoMelt and JdF (Figure 5), after removing the effects of
572   geometrical spreading via equation (4). As discussed in Section 3.1, the resulting structural
573   focusing correction ($\nabla^2 \tilde{\tau}$) should reflect focusing/defocusing due to lateral variations in
574   wavespeed along the ray path, both prior to the Rayleigh wave entering the array as well as
575   within the array footprint. We speculate that structural variations along the ray path prior to the
576   Rayleigh wave entering the OBS array should more strongly influence the overall
577   focusing/defocusing behavior (e.g., width of the distribution) because the OBS array footprint is
578   relatively small (only ~5° compared to tens of degrees of propagation between earthquake source
579   and the edge of the array). However, strong local velocity gradients within, or nearby, the array
580   will influence the finer details of the focusing patterns (e.g., skew of the distribution).

581   Overall, we observe that the distributions of focusing corrections at NoMelt are narrow,
582   strongly peaked around zero, and relatively symmetric for both data and synthetic, while at JdF
583   they are more broadly distributed indicating stronger focusing/defocusing. This is consistent with
584   more complicated source-receiver paths and waves that interact with the coastline at JdF as well
585   as the stronger velocity gradients present in the JdF region compared to NoMelt (Figure 3). In
586   detail, the distribution of focusing correction terms at 31 s period is skewed from zero at JdF, and
587   this skew in the real data (Figure 5d) occurs in the opposite sense from the skew in the synthetic
588   measurements (Figure 5a). A negative skew in the data indicates a tendency for the wavefield to
589   be focused upon entering the array, while a positive skew in the synthetics indicates defocusing.

590   The local velocity structure at JdF is likely one factor that contributes to the different
591   sense of skew for the focusing corrections measured from data and synthetics. Figure 5f shows
592   the phase velocity map estimated from equation (1) using our dense OBS observations, while
593   Figure 5c shows phase velocity predicted for S362ANI+CRUST2.0 using MINEOS. Perhaps
594   unsurprisingly, phase velocity measured from the real OBS data provides sharper constraints on
595   the low velocity JdF Ridge than does S362ANI, which was developed using basin-traversing
596   surface waves and body waves recorded at land stations (Kustowski et al., 2008). The presence
597   of the low-velocity JdF Ridge (< 3.7 km/s at 31 s period) along the western edge of the array,
598   together with the strongly biased event distribution (Figure 5g) with most events arriving from
599   the west, has a measurable impact on the focusing correction terms. Waves entering the array
600   from the west in the real Earth are preferentially focused by the slow velocities along the JdF
601   Ridge, while waves from those same events in the synthetic model are defocused by the fast
602   oceanic plate velocities to the west. Again, the focusing corrections for the real data are 4–5
603   times larger than for the synthetics, likely due to the smoothness of the synthetic model.
604   Regardless of the absence of the JdF Ridge in the synthetic model, the abrupt velocity contrast
605   associated with the ocean-continent transition still offers a useful scenario for testing the
606   limitations of Helmholtz tomography in the presence of strong elastic focusing.
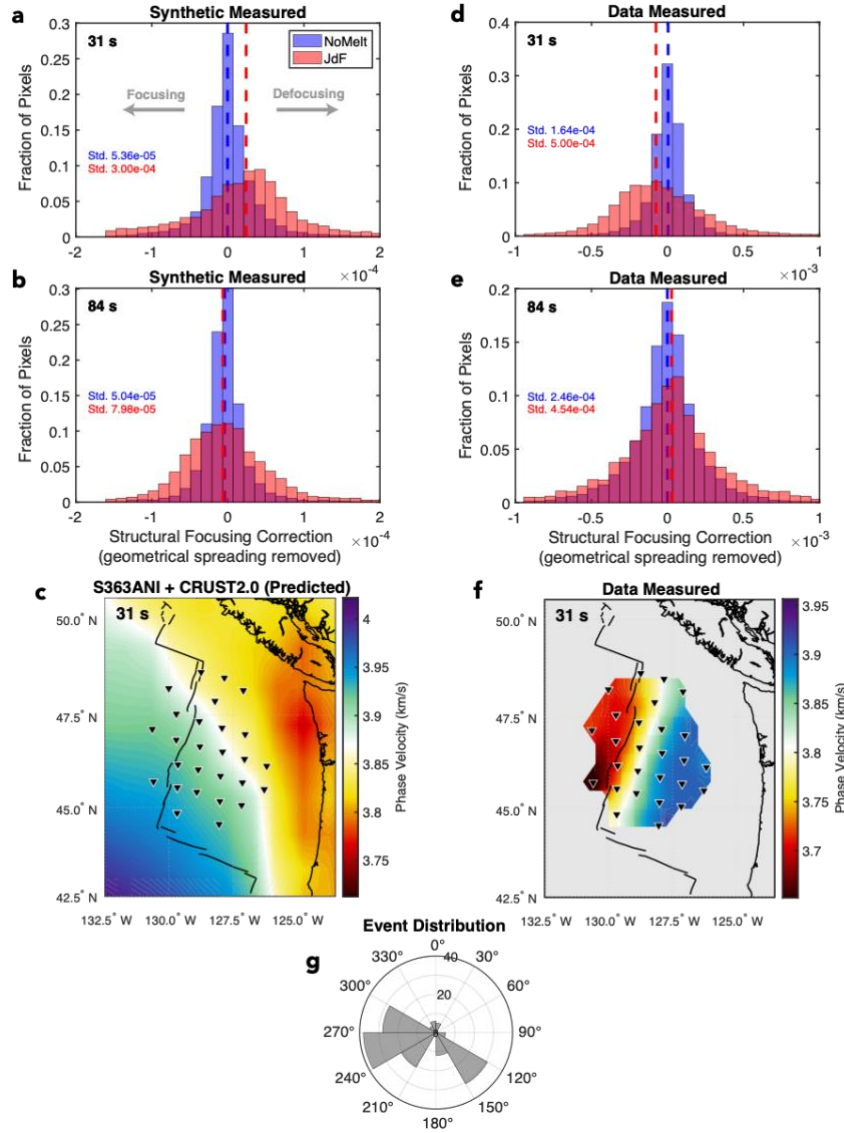
Figure 5. Distribution of structural focusing corrections, $\nabla^2 \tilde{\tau}$, at NoMelt (blue) and JdF (red) at (a) 31 s and (b) 84 s period measured from the synthetics using the true station geometries (left) and measurements from the real data (right). The effect of geometrical spreading has been removed via equation (4), and therefore wave focusing (negative values) and defocusing (positive values) are due to lateral variations in wavespeed along the propagation path. Vertical dashed lines show the median values of the distributions. (c) Synthetic phase velocity map at 31 s period, predicted using MINEOS as in Figure 3. (d–f) Same as a–c but for the real data. The measured phase velocity map in f) was produced by solving equation (1) and stacking over all events following Jin & Gaherty (2015). (g) Distribution of earthquake back azimuths at JdF, indicating most events originate from the west. Focusing behavior for data and synthetic is similar overall, except for at JdF at 31 s period, where the skew in correction terms for the real data indicates preferential focusing. This difference arises from the slow velocities along the western edge of the array associated with the JdF Ridge (f) — replaced by fast velocities in the synthetic model (c) — which focuses waves arriving from the west. Note the factor of 5 larger horizontal axis range in d,e compared to a,b.

623   5.2 Local site amplification

624   Before estimating local amplification from real data, we first use the synthetic travel time
625   and amplitude measurements to explore how well it can be recovered (Figures 6,7) using the
626   realistic event and OBS array geometries. Amplification is estimated from the azimuthal
627   variation of apparent attenuation (e.g., Figure 2; Figure 6a, Figure 7a) via equation (6). The
628   minimum of the sinusoid corresponds to the azimuth of maximum Rayleigh wave amplification,
629    $\beta > 1$ (likewise, the peak of the sinusoid indicates the azimuth of maximum deamplification, $\beta <$
630   1). For example, Figure 7a shows a minimum at ~60° for the synthetic JdF dataset, which
631   indicates that waves traveling northeast across the array are preferentially amplified. This is
632   reflected in the maps of β (Figure 7b). In this case, failing to account for amplification would
633   result in an apparent $\alpha < 0$ for observations at this propagation azimuth (i.e., wave amplitudes
634   *increase* with propagation distance). This demonstrates the importance of considering Rayleigh
635   wave amplification and attenuation together as well as the need for decent azimuthal coverage,
636   which is discussed further in Section 6.1.

637   We compare the amplification measured from synthetics to amplification predicted for
638   the 3-D model S362ANI+CRUST2.0, which we consider ground truth, at a desired pixel and
639   frequency from the following expressions (F. C. Lin et al., 2012)

640

$$\beta(x, y, \omega) = \left(\frac{cCI}{\overline{cCI}}\right)^{-\frac{1}{2}} \tag{12}$$

641

$$I = \frac{1}{U(a)^2} \int_0^a \rho(r)(U(r)^2 + V(r)^2)r^2 \, dr \tag{13}$$

642

643   where $\overline{cCI}$ is the average value within the array, therefore ensuring the mean of the predicted β
644   maps equals one as prescribed by the inversion (see section 3.2), and U and V are the vertical and
645   horizontal displacement eigenfunctions at position (x, y), respectively. The integral is carried out
646   from Earth's center to the seafloor at radius a.

647   Relative amplification (β) is recovered successfully from the synthetics at both NoMelt
648   (Figure 6) and JdF (Figure 7) at periods of 31 s and 84 s using the real station geometries and
649   event distributions. The correlation coefficient between measured and predicted values at both
650   locations is > 0.95, except for at NoMelt at 31 s period (R = 0.788; Figure 6d) for which
651   amplification and deamplification are weak (< 0.5%). Measured and predicted β maps at both
652   locations are roughly anti-correlated with the phase velocity maps shown in Figure 3, as
653   expected (F. C. Lin et al., 2012). Regions of amplification and deamplification tend to
654   correspond to slow and fast phase velocities, respectively, at least to first order. Amplification at
655   NoMelt varies by <1% due to the relatively modest velocity variations in S362ANI+CRUST2.0
656   at this location, whereas JdF shows variations of up to 5–7% amplification at 31 s period due to
657   the strong low velocities on the eastern edge of the array associated with the transition to
658   continental crust.

659   The highest predicted values of 31 s amplification at JdF of ~1.07 are slightly
660   underestimated by the synthetic measurements at ~1.05 (Figure 7d). This may be due to the
661   strongest amplification in the northeast being located at the edge of the map where fewer data are
662   available for binning within the surrounding 1.5° radius for the inversion. On the other hand,
663   strong deamplification values ($\beta < 1$) at the southwest edge of the map are very well recovered.
664   Another possibility is that a slight tradeoff exists between β and α due to the uneven azimuthal
665   coverage (Figure 5g). Although our 20° azimuthal binning procedure should lessen such biases,
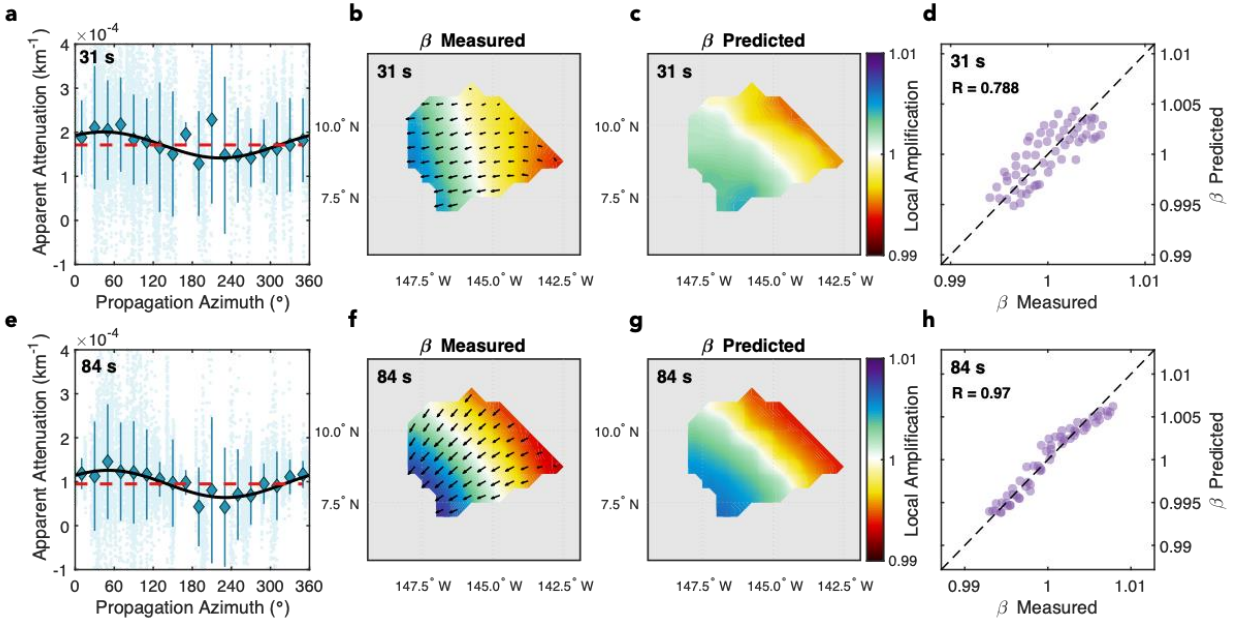666   azimuthal gaps inevitably exist for any given pixel in the map.

667

Figure 6. Synthetic recovery test of site amplification, β, at NoMelt. (a) Measurements of array-
averaged apparent attenuation (i.e., right-hand side of equation (6)) at 31 s period for all events
and pixels. Blue diamonds and error bars show the mean and standard deviation of points within
20° azimuthal bins, and the best fitting 1-D sinusoid is shown in black. The red dashed line
indicates the estimate of array-averaged anelastic attenuation, α. To estimate lateral variations in
amplification, we apply this same fitting procedure pixel-by-pixel (see Section 3.2 for details).
(b) Measured amplification maps via equations (7–8), where black vectors show the log
amplification gradient at each pixel obtained by binning measurements within a 1.5° radius and
performing fitting as in a). (c) Amplification predicted from the 3-D synthetic model
S362ANI+CRUST2.0 using equations (12–13). (d) Comparison of measured and predicted
amplification with correlation coefficient shown at the top left. (e–h) Same as a–d but for 84 s
period. Both measured and predicted amplification maps are normalized such that the average
within the array equals 1. Values of $\beta > 1$ correspond to amplification and $\beta < 1$ correspond to
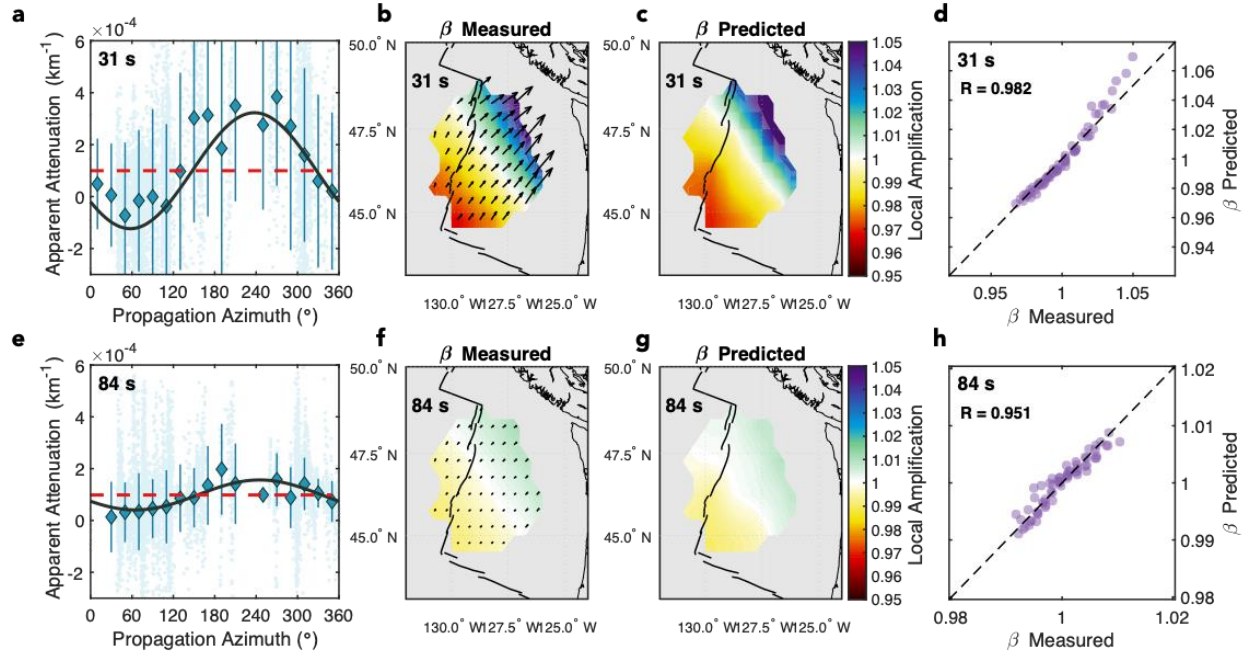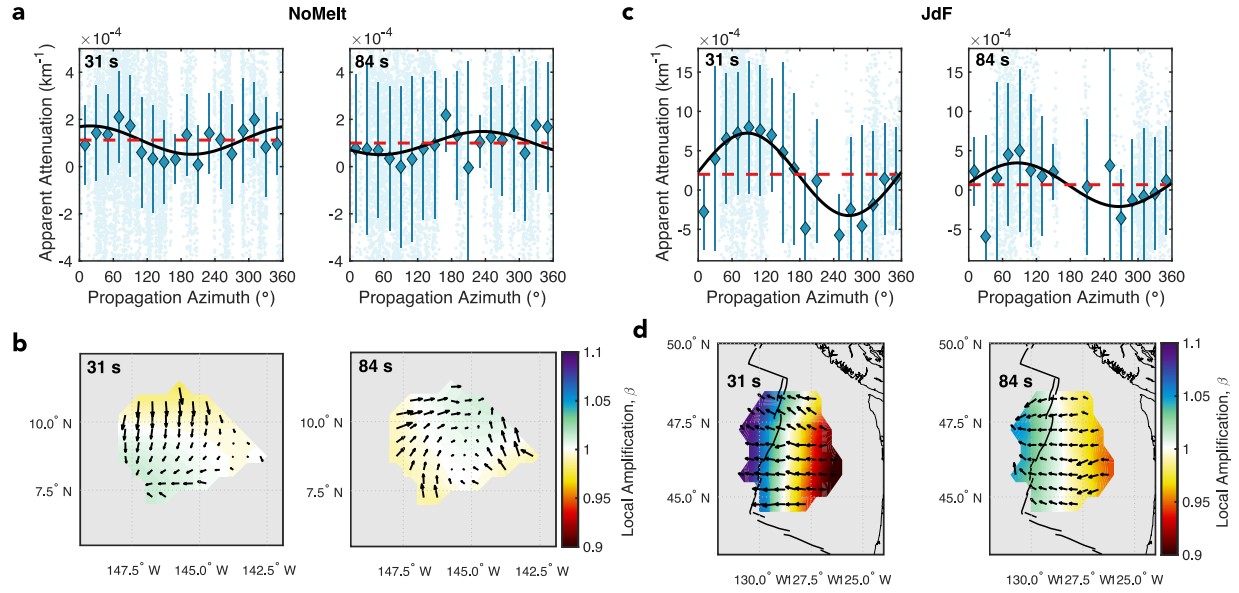deamplification.

682

Figure 7. Synthetic recovery test of site amplification, β, at JdF. See Figure 6 caption for details.

Figure 8 shows apparent attenuation and local amplification measured from the real data. The real observations reveal similar first order variations in β as the synthetic measurements and predictions at NoMelt and JdF with overall weak amplification/deamplification at NoMelt (Figure 8a,b) and stronger values at JdF (Figure 8c,d). The observed amplification variations at NoMelt are less spatially coherent at the two periods of interest, likely because the magnitudes of amplification and deamplification variations at NoMelt are small ($< 1\%$); indeed, the synthetic recovery tests demonstrate that weaker amplification variations are more difficult to resolve (Figure 6d). In contrast, β maps at JdF show strong variations in amplification ($> 10\%$ at 31 s period) that are spatially coherent at both periods of interest and correlate reasonably well with the low-velocity JdF Ridge (Figure 5f). These are among the first amplification maps observed in an oceanic setting and can be used together with complementary observations of Rayleigh wave phase velocity to better constrain shear and compressional velocities and density (e.g., Bowden et al., 2017; F. C. Lin et al., 2012), a future research direction discussed further in Section 6.3.

5.3 Array-averaged Rayleigh wave attenuation

Before estimating Rayleigh wave attenuation from real data, we first use the synthetic measurements to explore how well it can be recovered (Figure 9) using the realistic event and OBS array geometries. In general, we successfully recover the input 1-D Rayleigh wave attenuation at both NoMelt and JdF. To obtain these array-averaged estimates of attenuation at each period, we group together all apparent attenuation measurements for the whole study area (i.e., all events and pixels) and use our curve-fitting approach to solve for a single value of α (and $\nabla\beta/\beta$). Our implicit assumption that a single value of $\nabla\beta/\beta$ at each period can sufficiently represent the true variation in the maps in Figures 6 and 7 is reasonable given that β tends to vary smoothly (and simply) across our small study regions such that its gradient is relatively constant across the region. Violation of this assumption should result in more scatter around the

708   true α value, leading to larger α uncertainties, but should not significantly bias the array-
709   averaged α estimate.

710

Figure 8. Amplification maps observed from the real datasets. (a) Apparent attenuation
measurements (right-hand side of equation (6)) and (b) local amplification maps at NoMelt at 31
s and 84 s period. (c,d) Same as a,b but for JdF. Symbols as in Figures 6 & 7. Amplification
maps are normalized by the array-averaged value. Note the difference in the vertical axes in a)
and c).

716   Uncertainties in the recovered α values are generally smaller at NoMelt than JdF likely
717   owing to the weaker focusing and defocusing effects (Figure 5), weaker amplification variations
718   (Figure 6), and better azimuthal coverage (Figure 1). Uncertainties at JdF are especially large for
719   periods < 30–40 s likely due to the assumption of 1-D $\nabla\beta/\beta$ not being completely valid at these
720   periods as indicated by amplification gradients that tend to increase to the northeast (black
721   arrows in Figure 7b). It is also possible that the strong focusing and defocusing at these periods is
722   not perfectly accounted for, even for these noise-free synthetic tests, due to the complex focusing
723   patterns and difficulties resolving $\nabla^2\tau$ with sparse station coverage. Unaccounted for scattering
724   attenuation due to the abrupt velocity changes at the coastline may also contribute to these larger
725   uncertainties. We note that average attenuation is slightly underestimated at JdF at periods of 60–
726   80 s using the true station coverage, but it is well estimated at these periods using the idealized
727   0.5° station geometry (blue symbols in Figure 9), which suggests that the slight underestimate is
728   related to a lack of station coverage. Nevertheless, Figure 9 shows that the input attenuation
729   values are well recovered (to within uncertainty) at all periods from 20–150 s at both locations.

730   Attenuation recovered from the synthetics using the true station geometry (red symbols in
731   Figure 9) agrees with values recovered from the synthetics using the idealized 0.5° grid (blue
732   symbols), albeit with larger uncertainties. The smaller uncertainties across all periods for the
733   idealized station geometry likely reflect its ability to better recover the true focusing and
734   defocusing corrections. However, for periods <35 s at JdF, uncertainties are larger relative to
735   other periods also for the idealized geometry. This is consistent with the idealized geometry

736 encompassing a broad area (even larger than the true geometry) for which the assumption of 1-D
737 $\nabla\beta/\beta$ is not strictly valid, particularly at these shorter periods. In addition, we cannot rule out
738 that focusing correction terms are not perfectly resolved and could perhaps be improved with
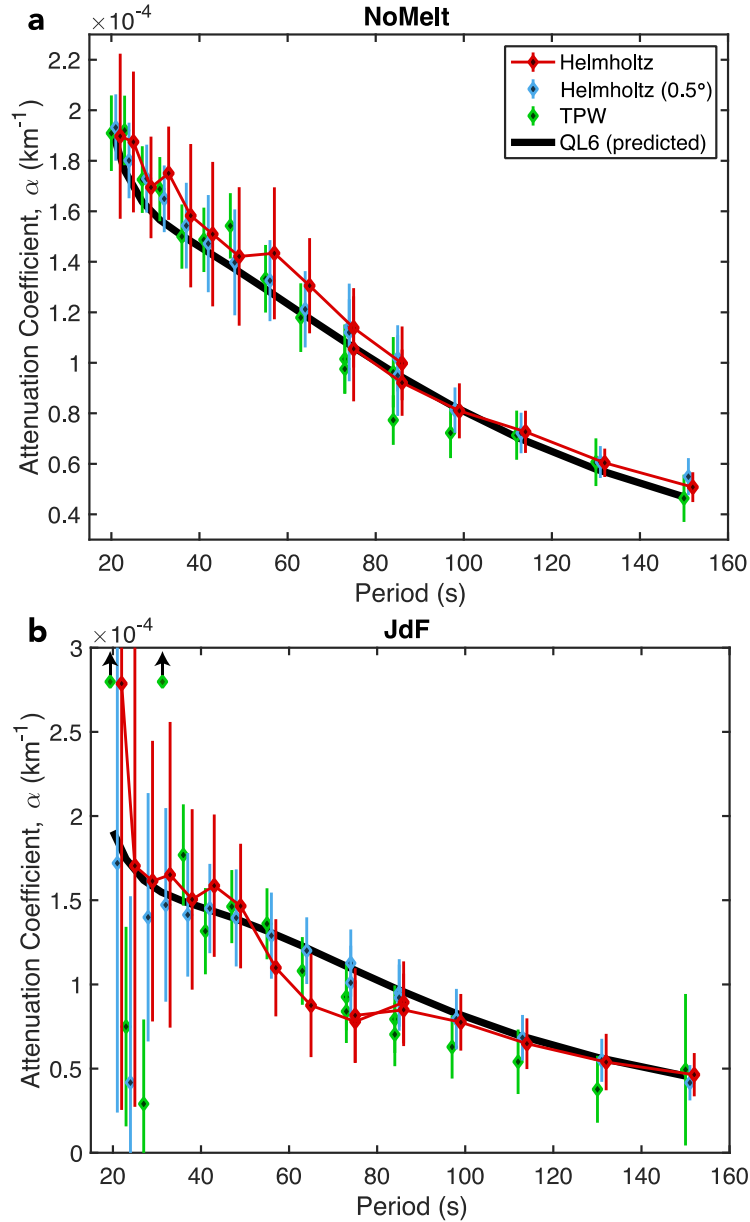739 finer station spacing ($< 0.5°$) and/or a weaker second-derivative smoothing constraint.

740

Figure 9. Recovery of synthetic 1-D attenuation coefficient, α, at (a) NoMelt and (b) JdF for
periods of 20–150 s. The predicted (target) attenuation values of QL6 (Durek & Ekström, 1996)
are shown in black. Red symbols show Helmholtz measurements that utilize the true station
geometry at each array. For comparison, the Helmholtz measurements for the idealized 0.5°×0.5°
station spacing are shown in blue, and green symbols show measurements from the two-plane
wave (TPW) inversion utilizing the phase and amplitude dataset for the true station geometry.
The upward pointing black arrows at 20 s and 31 s indicate TPW measurements that plot beyond
the vertical axis bounds ($\alpha \sim 26.9\times10^{-4}$ km^{-1} and 4.9×10^{-4} km^{-1}, respectively).

749 We compare our Helmholtz results with those of the TPW inversion (Forsyth & Li, 2005;
750 Yang & Forsyth, 2006) applied to the same synthetic phase and amplitude dataset using the true
751 station geometry (green symbols in Figure 9). Because the datasets are identical, differences
752 between the TPW and Helmholtz results are entirely due to differences in the theoretical
753 treatments of phase and amplitude. We find excellent agreement between Helmholtz and TPW at
754 all periods at NoMelt and at periods > 40 s at JdF, where focusing and defocusing are relatively
755 weak (Figure 5). For these scenarios, the wavefield can be sufficiently approximated by two
756 interfering plane waves. However, at JdF large differences appear at periods < 35 s, where TPW
757 is unable to recover the true 1-D attenuation within uncertainty. This breakdown of the TPW
758 technique indicates that the complex wavefield focusing and defocusing near the coastline in the
759 S362ANI+CRUST2.0 model cannot be sufficiently described by the interference of two plane
760 waves.

761 The 1-D attenuation coefficients measured from the real datasets are presented in Figure
762 10 for NoMelt (blue) and JdF (red). Attenuation is higher at JdF than NoMelt for periods < 70 s,
763 whereas the opposite is true for periods > 90 s. To first order, our new observations at the two
764 regions compare favorably with previous measurements using the TPW technique (lighter
765 colored symbols in Figure 10), but important differences exist. Our observations show higher
766 attenuation at all periods at NoMelt and slightly lower attenuation on average at most periods at
767 JdF. Attenuation at NoMelt is slightly higher than PREM values at all periods > 30 s, whereas
768 JdF shows much higher attenuation than PREM at periods < 80 s and comparable attenuation at
769 periods > 80 s. Attenuation from global model QRFSI12 (Dalton et al., 2008; Dalton & Ekström,
770 2006) sampled within the NoMelt and JdF regions is roughly consistent with our new
771 measurements at > 50 s period, but we find bigger differences in attenuation between the two
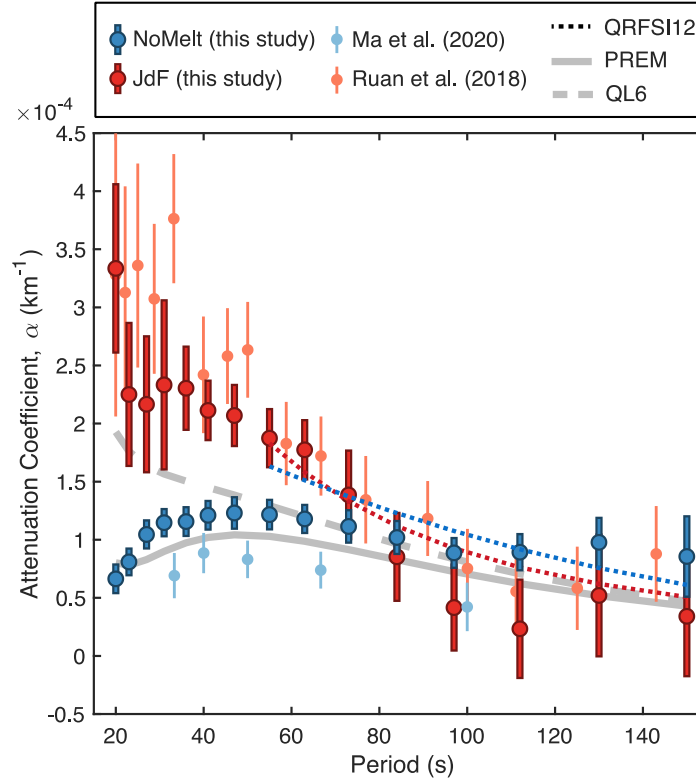772 regions than QRFSI12.
773

774

Figure 10. Measured 1-D attenuation coefficients for periods ranging from 20–150 s for NoMelt
(blue) and JdF (red). For comparison, TPW-derived measurements from two previous studies are
shown for NoMelt (Ma et al., 2020) and JdF (Ruan et al., 2018). 1-D global models QL6 (Durek
& Ekström, 1996) and PREM (Dziewonski & Anderson, 1981) are shown in gray. Dotted lines
show attenuation from the 3-D global model QRFSI12 (Dalton et al., 2008) estimated at the
center of each deployment location using MINEOS. Error bars represent 2σ uncertainty.

781   5.4 Shear attenuation profiles

782   We invert our new Helmholtz measurements of Rayleigh wave attenuation for profiles of
783 upper mantle shear attenuation at NoMelt and JdF (Figure 11). Frequency-dependent Rayleigh
784 wave attenuation, $Q^{-1}(\omega)$, is related to shear attenuation, $Q_\mu^{-1}(r)$, and bulk attenuation, $Q_\kappa^{-1}(r)$,
785 as a function of radius r through the expression (Dziewonski & Anderson, 1981)

786

$$Q^{-1}(\omega) = \int_0^a \left[\mu(r)K_\mu(\omega,r)\, Q_\mu^{-1}(r) + \kappa(r)K_\kappa(\omega,r)\, Q_\kappa^{-1}(r) \right] dr \qquad (14)$$

787

788 where μ and κ are the shear and bulk moduli, respectively, and K_μ and K_κ are the Fréchet kernels
789 describing sensitivity of Rayleigh waves to changes in μ and κ, respectively. Since both upper-
790 mantle bulk attenuation and the sensitivity of Rayleigh waves to it are much smaller than is the
791 case for shear attenuation, we fix Q_κ^{-1} to PREM values (Dziewonski & Anderson, 1981). We

792   perform a regularized least-squares inversion of equation (14) for Q_μ^{-1} in the depth range 0–250
793   km with norm damping and second derivative smoothing, using MINEOS to calculate the
794   sensitivity kernels (see Supplementary Figure S4). The sensitivity kernels primarily depend on
795   the shear velocity structure, and therefore we first invert average phase velocity dispersion data
796   for a smooth 1-D shear velocity profile at each location. We then invert for Q_μ^{-1} using the two-
797   layer NoMelt attenuation model of Ma et al. (2020) as the starting model for both NoMelt and
798   JdF, adjusting the water depth accordingly, but do not find a strong dependence on assumed
799   starting attenuation model. Crustal Q_μ is held fixed at 1400. Model uncertainties are estimated
800   through a bootstrap resampling approach in which the attenuation data are randomly perturbed
801   within their uncertainty bounds and reinverted. This is repeated 500 times producing an
802   ensemble of models, and the 1σ uncertainties are estimated from the middle 68% of the
803   ensemble.

804   The resulting 1-D models of shear attenuation and their fit to the data are shown in Figure
805   11. Shear attenuation at NoMelt is characterized by a low attenuation lithospheric layer ($Q_\mu >$
806   1500) overlying a high attenuation asthenospheric layer ($Q_\mu \sim$ 50–70) with a transition between
807   the two occurring from ~50–100 km depth. At JdF, we observe a broad peak in attenuation ($Q_\mu \sim$
808   50–60) centered at a depth of 100–130 km, bounded above and below by low attenuation regions
809   ($Q_\mu > 200$). In both cases, uncertainties increase with depth due to the larger uncertainties at
810   longer periods.

811   **6 Discussion**

812   6.1 Advantages and limitations of Helmholtz tomography

813   We demonstrate that Helmholtz tomography can recover 1-D Rayleigh wave attenuation
814   and 2-D maps of site amplification using typical OBS array geometries, even in the presence of
815   strong elastic focusing and defocusing due to coastline effects. The power of the approach lies in
816   its ability to account for complex patterns of elastic focusing without imposing strict physical
817   assumptions about the nature of wavefield interference. Rather, the focusing behavior is directly
818   observed and accounted for via $\nabla^2\tau$. In contrast, the TPW approach imposes a physical limitation
819   on wavefield complexity. This approximation is sufficient in many settings, such as structurally
820   homogeneous regions of the ocean basins far away from continents, like NoMelt, but it may
821   break down in more complex areas such as JdF, where the coastline has a large influence on
822   multipathing behavior at periods < 35 s (Figure 9b). On the other hand, an important limitation
823   of Helmholtz tomography is that it requires decent station coverage in two dimensions in order to
824   accurately resolve the gradient and Laplacian fields in equation (6). Sharp lateral variations in
825   these fields are challenging to resolve given the smooth regularization scheme used (equation 10)
826   and/or limitations in station coverage. In situations where station coverage is lacking, the TPW
827   approach may be advantageous as the assumption of two interfering plane waves provides a solid
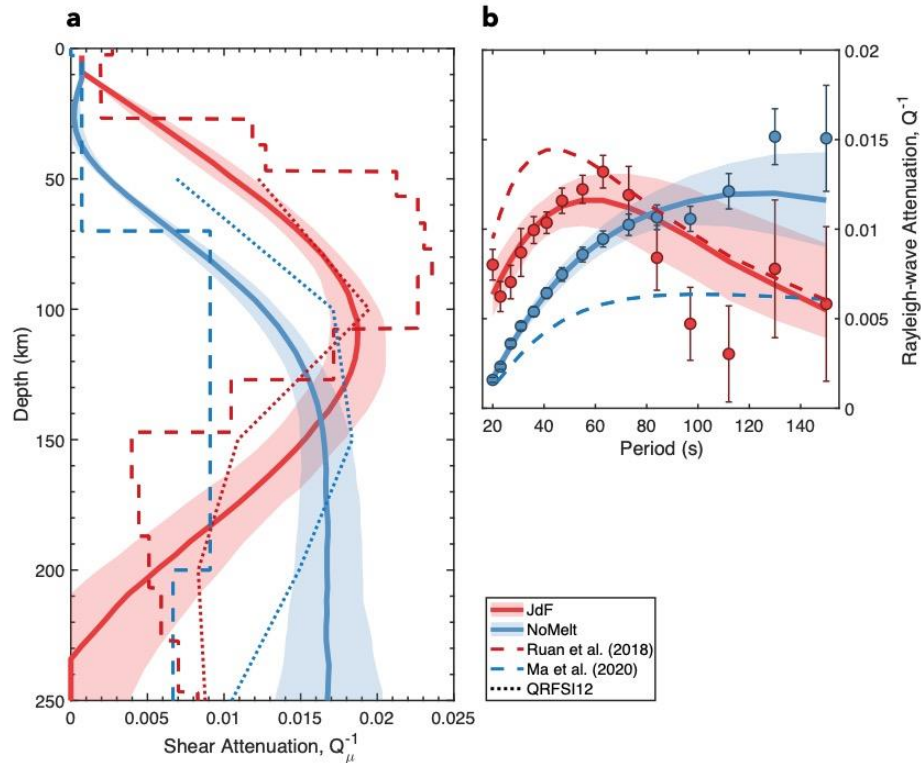828   physical basis for extrapolating wavefield behavior across data-poor regions.

829

Figure 11. (a) Inversion for 1-D shear attenuation profiles at NoMelt (blue) and JdF (red). The solid lines and shaded regions show the median and 68% confidence interval, respectively, from bootstrap resampling. (b) Model fit to our data (filled circles with 1σ error bars). Previous 1-D shear attenuation models and predictions for NoMelt (Ma et al., 2020) and JdF (Ruan et al., 2018) are shown by dashed lines. Dotted lines show attenuation profiles from global model QRFSI12 (Dalton et al., 2008) extracted from the approximate deployment locations.

Helmholtz tomography is able to simultaneously account for both attenuation and site amplification via the mean and azimuthal variation of apparent amplitude decay, respectively. Accounting for local site amplification when estimating attenuation is especially important if amplification variations are strong and/or azimuthal gaps exist in the dataset. Both sources of bias can be understood by considering the synthetic JdF dataset as an example (Figure 7a,e). Apparent attenuation varies strongly with azimuth, especially at 31 s, and thus a dataset dominated by waves that propagate to the northeast at 60° azimuth would lead to attenuation estimates at JdF that are biased low (negative even), whereas the opposite would be true of a dataset dominated by waves propagating to the southwest at 240°. Such biases will increase with the magnitude of amplification variations (compare Figure 7a and 7e). Therefore, a decent azimuthal distribution of teleseismic earthquakes is necessary to prevent tradeoffs between attenuation and site amplification, especially if amplification variations are strong.

In this study, we focus on characterizing the average Rayleigh wave attenuation within small seismic arrays. Solving for 2-D maps of Rayleigh wave attenuation is desirable but challenging due to the issues outlined above, such as limited station coverage and potential tradeoffs due to uneven azimuthal distribution of earthquakes. Indeed, previous studies that utilized data from the USArray encountered challenges resolving detailed 2-D attenuation maps (F. C. Lin et al., 2012) and required both masking and spatial smoothing up to ~3° radius (Bao et

854 al., 2016). Such smoothing would effectively smear away any lateral variation within a typical
855 OBS array on the order of ~500x500 km^2. We therefore focus on 1-D array-average estimates of
856 attenuation. As OBS arrays are typically small, 1-D attenuation is useful for characterizing OBS
857 deployment regions. Although we focus here on applications at smaller scale OBS arrays, the
858 methodology can be extended to similarly sized arrays in continental settings. For larger arrays
859 such as the USArray, one could estimate 1-D attenuation within "subarrays" representing regions
860 that are expected to contain little lateral heterogeneity. Additional synthetic testing using realistic
861 wave propagation through laterally varying 3-D anelastic media is required to evaluate the ability
862 to reliably resolve lateral variations in Rayleigh wave attenuation within larger arrays.

863   6.2 Comparison to previous attenuation studies

864   While our new observations of shear attenuation at NoMelt and JdF broadly resemble
865 previous observations, important differences do exist. The approximate two-layer structure that
866 we observe at NoMelt with a transition from low to high attenuation at 50–100 km depth is
867 consistent with the two-layer model of Ma et al. (2020) with the lithosphere-asthenosphere
868 boundary at 70 km depth; however, in the earlier study the asthenospheric layer shows lower
869 attenuation (Q_μ ~ 110) than we find here (Q_μ ~ 50–70), which underpredicts our Rayleigh wave
870 attenuation observations at periods > 25 s (blue dashed line in Figure 11b). Compared to the
871 NoMelt region in global model QRFSI12 (Dalton et al., 2008), our NoMelt model is slightly less
872 attenuating from 50–150 km and is slightly more attenuating from 200–250 km. However, the
873 general agreement is exceptional given the broad sensitivities associated with global modeling
874 compared to our local estimates.

875   The high attenuation peak at 100–130 km depth that we observe at JdF resembles that of
876 Ruan et al. (2018), but the attenuation peak in their model is both shallower (50–100 km) and
877 stronger (Q_μ ~ 46), overpredicting our attenuation observations for periods < 60 s (red dashed
878 line in Figure 11b). The deeper high attenuation region in our model is more consistent with
879 body-wave observations that imply a low viscosity melt column extending to ~150 km below the
880 JdF Ridge (Eilon & Abers, 2017). The low attenuation region at >200 km depth in our model
881 (Q_μ > 200) appears less attenuating than Ruan et al. (2018) at first glance, but values are
882 consistent to within uncertainty (see their Figure 2c). Our observations agree well with QRFSI12
883 at depths of 50–150 km, but we observe lower attenuation from 200–250 km.

884   Differences between our estimates of Q_μ at NoMelt and JdF and previous observations
885 are primarily related to inconsistencies in the Rayleigh wave attenuation measurements (Figure
886 10), rather than in the inversion procedure. This point is demonstrated by the large misfit
887 between previous model predictions of Rayleigh wave attenuation and our observations in Figure
888 11b. As the previous attenuation measurements of Ruan et al. (2018) and Ma et al. (2020) were
889 made using the TPW method, a key question is whether these differences can be attributed to our
890 use of Helmholtz tomography or whether they arise from the raw amplitude and/or phase
891 measurements themselves. Our synthetic tests show that Helmholtz and TPW yield similar
892 attenuation measurements (at periods >35 s, where focusing corrections are smaller), when
893 applied to the same amplitude and phase dataset (Figure 9). A similar result is found using the
894 real data: Helmholtz and TPW attenuation measurements agree to within uncertainty when
895 applied to the same amplitude and phase dataset (pink symbols in Supplementary Figure S3).
896 This suggests, albeit indirectly, that differences in our revised attenuation estimates arise from
897 differences in the raw single-station amplitude measurements and/or event distribution and not

898   the chosen theoretical framework used to interpret these amplitudes in terms of attenuation (i.e.,
899   Helmholtz versus TPW). We use the cross-correlation based ASWMS tool of Jin & Gaherty
900   (2015) to measure station amplitude and differential phase, while previous TPW studies used a
901   single-station Fourier transform (FT) based method (Forsyth & Li, 2005) to measure amplitude
902   and phase. Both techniques involve time windowing and narrow-band filtering of the waveform,
903   but windowing in ASWMS is performed automatically based on broadband Rayleigh wave
904   energy (narrow-band filtering occurs after cross-correlation), whereas for the FT method,
905   narrow-band filters are applied before windowing and user input is required to manually select
906   the edges of each window. Given these differences, it is difficult to determine at what stage in
907   the measurement procedures the amplitude measurements might diverge. We emphasize that
908   phase velocity measurements using ASWMS and FT are equivalent to within uncertainty (see
909   Figure 4a in Ma et al., 2020), indicating that phase is consistent between the two measurement
910   techniques.

911   Both the Helmholtz and TPW methods applied to ASWMS amplitude and phase
912   measurements are able to recover the true attenuation (and amplification) values from realistic
913   SPECFEM3D GLOBE synthetic seismograms, providing confidence in our revised attenuation
914   estimates at JdF and NoMelt. An advantage of our study is that we treat the JdF and NoMelt
915   datasets identically throughout both the measurement and inversion procedures, and therefore,
916   differences in attenuation observed between the two locations are driven strictly by the data and
917   not by ad hoc choices made within the analysis. In a future study, we will interpret these updated
918   profiles of Q_μ alongside profiles of shear velocity to quantify temperature, melt fraction, and
919   grain size in the oceanic asthenosphere.

920   6.3 Site amplification: A new observable in the oceans

921   Our observations of local site amplification, β, at JdF and NoMelt are among the first of
922   their kind in an oceanic setting. Only a handful of previous studies have measured Rayleigh
923   wave amplification at periods > 20 s (Bao et al., 2016; Bowden et al., 2017; Eddy & Ekström,
924   2014, 2020; F. C. Lin et al., 2012), and these studies all used data from the USArray. One study
925   that we are aware of has inverted Rayleigh wave amplification measurements for shear velocity
926   structure, and this too was carried out in the western U.S. (Schardong et al., 2019). The
927   sensitivities of Rayleigh wave amplification to shear velocity (V_S), compressional velocity (V_P),
928   and density (ρ) are complementary to that of phase velocity and may be used to refine models of
929   3-D Earth structure (Bowden et al., 2017; F. C. Lin et al., 2012; Schardong et al., 2019).
930   Amplification displays opposite sensitivities to shear and compressional velocities at shallow
931   depths, implying that V_P/V_S may be especially well resolved by amplification measurements (F.
932   C. Lin et al., 2012). In contrast to phase and group velocity, the amplification sensitivity kernels
933   for V_S have multiple zero-crossings and therefore should better resolve sharp gradients in shear
934   velocity with depth (Babikoff, 2022; Dalton & Babikoff, 2021; F. C. Lin et al., 2012).

935   Our synthetic recovery tests (Figures 6 & 7) and application to the real datasets (Figure 8)
936   demonstrate that amplification can be measured at typical OBS array geometries using
937   Helmholtz tomography. Strong amplification observed along the JdF Ridge approximately
938   coincides with slow phase velocities (Figure 5f), indicating that they can be inverted together to
939   refine shallow Earth structure. In particular, improved shallow estimates of V_P/V_S at the JdF
940   Ridge could shed light on the organization of melt and crustal accretion processes as well as
941   shallow cracks and hydrothermal circulation (Kim et al., 2019; Lee et al., 2017; Takei, 2002).

942   We reemphasize that β is a relative quantity with mean value equal to one within the array, and
943   thus, an inversion of amplification for structural parameters V_S, V_P, and ρ must also preserve the
944   array average. Joint inversion of amplification and phase velocity maps for crust and mantle
945   properties at JdF will be the topic of a future study.

946   **7 Conclusions**

947   This manuscript demonstrates the first application of Helmholtz attenuation tomography
948   in an oceanic setting, yielding new measurements of Rayleigh wave attenuation and local site
949   amplification at 20–150 s period at the NoMelt and JdF regions. Using realistic simulations of
950   wave propagation through 3-D elastic structure, we show that the technique faithfully accounts
951   for wavefield focusing and defocusing, including in extreme scenarios associated with coastline
952   effects. The focusing and defocusing corrections measured using the real dataset are qualitatively
953   similar to the synthetics but are larger in amplitude, likely due to the smooth global model used
954   to generate the synthetic dataset. The methodology has been implemented as an add-on to the
955   ASWMS software package (Jin & Gaherty, 2015; see Open Research statement), offering a new
956   tool for estimating Rayleigh wave attenuation and amplification across regional-scale arrays that
957   has been validated using realistic synthetic seismograms. Although our focus is on applications
958   at smaller scale OBS arrays (~500x500 km^2), the technique can be extended to comparable
959   datasets on land.

960   Both 1-D attenuation and 2-D site amplification are successfully recovered in the
961   synthetic tests at NoMelt and JdF, indicating that the array geometries and earthquake
962   distributions are sufficient for resolving tradeoffs between attenuation and site amplification.
963   When applied to the real data, our measurements of Rayleigh wave attenuation at NoMelt and
964   JdF revise previous estimates derived using the TPW method. Our preliminary inversions of
965   Rayleigh wave attenuation for 1-D profiles of shear attenuation, Q_μ, reveal significantly higher
966   attenuation in the asthenosphere at NoMelt and a deeper high-attenuation region at JdF compared
967   to previous studies. Maps of site amplification at JdF show high amplification (> 10% at 31 s
968   period) along the low-velocity JdF Ridge, providing a new observable that can be inverted
969   alongside phase velocity to improve models of shallow subsurface structure at the mid-ocean
970   ridge.

971   **Acknowledgments**

983   **Open Research**

984 The methodology described in this manuscript is implemented as an add-on to the MATLAB-based

985 Automated Surface-Wave Measurement System (ASWMS) of Jin & Gaherty (2015) and is hosted on

986 GitHub (https://github.com/jbrussell/ASWMS-Q.git); the Mapping Toolbox is required. The maps in

987 Figure 1 were generated using the Python-based PyGMT software (https://www.pygmt.org/). The

988 SPECFEM3D_GLOBE software used to generate the synthetic datasets can be downloaded here:

989 https://github.com/geodynamics/specfem3d_globe.git. The Automated Tilt and Compliance Removal

990 (ATaCR) software can be accessed here: https://github.com/helenjanisz/ATaCR.git. Data used in

991 this manuscript were retrieved from the Incorporated Research Institutions for Seismology (IRIS)

992 Data Management Center (DMC) under network codes ZA (NoMelt) and 7D (Cascadia Initiative;

993 Juan de Fuca).

994 **References**

995 Adenis, A., Debayle, E., & Ricard, Y. (2017a). Attenuation tomography of the upper mantle.
996   *Geophysical Research Letters*, *44*, 7715–7724. https://doi.org/10.1002/2017GL073751

997 Adenis, A., Debayle, E., & Ricard, Y. (2017b). Seismic evidence for broad attenuation anomalies
998   in the asthenosphere beneath the Pacific Ocean. *Geophysical Journal International*, *209*,
999   1677–1698. https://doi.org/10.1093/gji/ggx117

1000 Babikoff, J. (2022). *Imaging the lithosphere and asthenosphere beneath North America with*
1001   *Rayleigh wave phase velocity and amplification*. Brown University.

1002 Bao, X., Dalton, C. A., Jin, G., Gaherty, J. B., & Shen, Y. (2016). Imaging Rayleigh wave
1003   attenuation with USArray. *Geophysical Journal International*, *206*(1), 241–259.
1004   https://doi.org/10.1093/gji/ggw151

1005 Bassin, C., Laske, G., & Masters, G. (2000). The Current Limits of Resolution for Surface Wave
1006   Tomography in North America. *EOS Trans AGU*, *81*, F897.

1007 Bell, S. W., Ruan, Y., & Forsyth, D. W. (2016). Ridge asymmetry and deep aqueous alteration at
1008   the trench observed from Rayleigh wave tomography of the Juan de Fuca plate. *Journal of*
1009   *Geophysical Research : Solid Earth*, *121*, 7298–7321.
1010   https://doi.org/10.1002/2016JB012990.Received

1011 Bowden, D. C., Tsai, V. C., & Lin, F. C. (2017). Amplification and Attenuation Across USArray
1012   Using Ambient Noise Wavefront Tracking. *Journal of Geophysical Research: Solid Earth*,
1013   *122*, 10,086-10,101. https://doi.org/10.1002/2017JB014804

1014 Byrnes, J. S., Toomey, D. R., Hooft, E. E. E., Nábělek, J., & Braunmiller, J. (2017). Mantle
1015   dynamics beneath the discrete and diffuse plate boundaries of the Juan de Fuca plate:
1016   Results from Cascadia Initiative body wave tomography. *Geochemistry, Geophysics,*
1017   *Geosystems*, *18*, 2906–2929. https://doi.org/10.1002/2017GC006980

Chevrot, S., & Lehujeur, M. (2022). Eikonal surface wave tomography with smoothing splines— application to Southern California. *Geophysical Journal International*, *229*(3), 1927–1941. https://doi.org/10.1093/gji/ggac034

Crawford, W. C., & Webb, S. C. (2000). Identifying and Removing Tilt Noise from Low Frequency (<0.1 Hz) Seafloor Vertical Seismic Data. *Bulletin of the Seismological Society of America*, *90*(4), 952–963. https://doi.org/10.1785/0119990121

Dalton, C. A., & Babikoff, J. (2021). Rayleigh wave amplification: sensitivity to elastic structure and application to Alaskan crust and upper mantle. In *AGU Fall Meeting Abstracts*. New Orleans.

Dalton, C. A., & Ekström, G. (2006). Global models of surface wave attenuation. *Journal of Geophysical Research: Solid Earth*, *111*(5), 1–19. https://doi.org/10.1029/2005JB003997

Dalton, C. A., & Faul, U. H. (2010). The oceanic and cratonic upper mantle: Clues from joint interpretation of global velocity and attenuation models. *Lithos*, *120*, 160–172. https://doi.org/10.1016/j.lithos.2010.08.020

Dalton, C. A., Ekström, G., & Dziewonski, A. M. (2008). The global attenuation structure of the upper mantle. *Journal of Geophysical Research*, *113*, 1–24. https://doi.org/10.1029/2007JB005429

Debayle, E., Bodin, T., Durand, S., & Ricard, Y. (2020). Seismic evidence for partial melt below tectonic plates. *Nature*, *586*, 555–559. https://doi.org/10.1038/s41586-020-2809-4

Durek, J. J., & Ekström, G. (1996). A radial model of anelasticity consistent with long-period surface-wave attenuation. *Bulletin of the Seismological Society of America*, *86*, 144–158.

Dziewonski, A. M., & Anderson, D. L. (1981). Preliminary reference Earth model. *Physics of the Earth and Planetary Interiors*, *25*, 297–356.

Eddy, C. L., & Ekström, G. (2014). Local amplification of Rayleigh waves in the continental United States observed on the USArray. *Earth and Planetary Science Letters*, *402*, 50–57. https://doi.org/10.1016/j.epsl.2014.01.013

Eddy, C. L., & Ekström, G. (2020). Comparisons between measurements and predictions of Rayleigh wave amplification across the contiguous United States. *Physics of the Earth and Planetary Interiors*, *299*, 106407. https://doi.org/10.1016/j.pepi.2019.106407

Eilon, Z. C., & Abers, G. A. (2017). High seismic attenuation at a mid-ocean ridge reveals the distribution of deep melt. *Science Advances*, *3*, e1602829. https://doi.org/10.1126/sciadv.1602829

Eilon, Z. C., & Forsyth, D. W. (2020). Depth-Dependent Azimuthal Anisotropy Beneath the Juan de Fuca Plate System. *Journal of Geophysical Research: Solid Earth*, *125*, e2020JB019477. https://doi.org/10.1029/2020JB019477

Ekström, G., Nettles, M., & Dziewoński, A. M. (2012). The global CMT project 2004-2010: Centroid-moment tensors for 13,017 earthquakes. *Physics of the Earth and Planetary Interiors*, *200–201*, 1–9. https://doi.org/10.1016/j.pepi.2012.04.002

Faul, U. H., & Jackson, I. (2005). The seismological signature of temperature and grain size variations in the upper mantle. *Earth and Planetary Science Letters*, *234*, 119–134.

1058   https://doi.org/10.1029/2001jb001225

1059 Forsyth, D. W., & Li, A. (2005). Array Analysis of Two-Dimensional Variations in Surface
1060   Wave Phase Velocity and Azimuthal Anisotropy in the Presence of Multipathing
1061   Interference. *Seismic Earth: Array Analysis of Broadband Seismograms Geophysical*
1062   *Monograph Series*, *157*, 81–97.

1063 Hariharan, A., Dalton, C. A., Ma, Z., & Ekström, G. (2020). Evidence of Overtone Interference
1064   in Fundamental-Mode Rayleigh Wave Phase and Amplitude Measurements. *Journal of*
1065   *Geophysical Research: Solid Earth*, *125*, 1–17. https://doi.org/10.1029/2019JB018540

1066 Hariharan, A., Dalton, C. A., Babikoff, J., & Ekström, G. (2022). Controls on surface wave
1067   overtone interference. *Geophysical Journal International*, *228*, 1665–1683.
1068   https://doi.org/10.1093/gji/ggab424

1069 Havlin, C., Holtzman, B. K., & Hopper, E. (2021). Inference of thermodynamic state in the
1070   asthenosphere from anelastic properties, with applications to North American upper mantle.
1071   *Physics of the Earth and Planetary Interiors*, *314*, 106639.
1072   https://doi.org/10.1016/j.pepi.2020.106639

1073 Hawley, W. B., Allen, R. M., & Richards, M. A. (2016). Tomography reveals buoyant
1074   asthenosphere accumulating beneath the Juan de Fuca plate. *Science*, *353*(6306), 1406–
1075   1408. https://doi.org/10.1126/science.aad8104

1076 Jackson, I., & Faul, U. H. (2010). Grainsize-sensitive viscoelastic relaxation in olivine: Towards
1077   a robust laboratory-based model for seismological application. *Physics of the Earth and*
1078   *Planetary Interiors*, *183*, 151–163. https://doi.org/10.1016/j.pepi.2010.09.005

1079 Janiszewski, H. A., Gaherty, J. B., Abers, G. A., Gao, H., & Eilon, Z. C. (2019). Amphibious
1080   surface-wave phase-velocity measurements of the Cascadia subduction zone. *Geophysical*
1081   *Journal International*, *217*(3), 1929–1948. https://doi.org/10.1093/gji/ggz051

1082 Jin, G., & Gaherty, J. B. (2015). Surface wave phase-velocity tomography based on multichannel
1083   cross-correlation. *Geophysical Journal International*, *201*(3), 1383–1398.
1084   https://doi.org/10.1093/gji/ggv079

1085 Karaoğlu, H., & Romanowicz, B. (2018). Inferring global upper-mantle shear attenuation
1086   structure by waveform tomography using the spectral element method. *Geophysical Journal*
1087   *International*, *213*, 1536–1558. https://doi.org/10.1093/gji/ggy030

1088 Kim, E., Toomey, D. R., Hooft, E. E. E., Wilcock, W. S. D., Weekly, R. T., Lee, S. M., & Kim,
1089   Y. H. (2019). Upper Crustal Vp/Vs Ratios at the Endeavour Segment, Juan de Fuca Ridge,
1090   From Joint Inversion of P and S Traveltimes: Implications for Hydrothermal Circulation.
1091   *Geochemistry, Geophysics, Geosystems*, *20*, 208–229.
1092   https://doi.org/10.1029/2018GC007921

1093 Komatitsch, D., & Tromp, J. (2002a). Spectral-element simulations of global seismic wave
1094   propagation—II. Three-dimensional models, oceans, rotation and self-gravitation.
1095   *Geophysical Journal International*, *150*, 303–318. https://doi.org/10.1046/j.1365-
1096   246X.2002.01653.x

1097 Komatitsch, D., & Tromp, J. (2002b). Spectral-element simulations of global seismic wave
1098   propagation - I. Validation. *Geophysical Journal International*, *149*(2), 390–412.

1099   https://doi.org/10.1046/j.1365-246X.2002.01653.x

1100   Kustowski, B., Ekstro, G., & Dziewonski, A. M. (2008). Anisotropic shear-wave velocity
1101   structure of the Earth's mantle: A global model. *Journal of Geophysical Research*, *113*, 1–
1102   23. https://doi.org/10.1029/2007JB005169

1103   Langston, C. A. (2007a). Spatial gradient analysis for linear seismic arrays. *Bulletin of the*
1104   *Seismological Society of America*, *97*(1 B), 265–280. https://doi.org/10.1785/0120060100

1105   Langston, C. A. (2007b). Wave gradiometry in the time domain. *Bulletin of the Seismological*
1106   *Society of America*, *97*(3), 926–933. https://doi.org/10.1785/0120060152

1107   Langston, C. A. (2007c). Wave gradiometry in two dimensions. *Bulletin of the Seismological*
1108   *Society of America*, *97*(2), 401–416. https://doi.org/10.1785/0120060138

1109   Lee, A. L., Walker, A. M., Lloyd, G. E., & Torvela, T. (2017). Geochemistry, Geophysics,
1110   Geosystems. *Geochemistry, Geophysics, Geosystems*, *18*, 1090–1110.
1111   https://doi.org/10.1002/2016GC006705.Received

1112   Lin, F.-C., & Ritzwoller, M. H. (2011). Helmholtz surface wave tomography for isotropic and
1113   azimuthally anisotropic structure. *Geophysical Journal International*, *186*(3), 1104–1120.
1114   https://doi.org/10.1111/j.1365-246X.2011.05070.x

1115   Lin, F.-C., Ritzwoller, M. H., & Snieder, R. (2009). Eikonal tomography: surface wave
1116   tomography by phase front tracking across a regional broad-band seismic array.
1117   *Geophysical Journal International*, *177*(3), 1091–1110. https://doi.org/10.1111/j.1365-
1118   246X.2009.04105.x

1119   Lin, F. C., Tsai, V. C., & Ritzwoller, M. H. (2012). The local amplification of surface waves: A
1120   new observable to constrain elastic velocities, density, and anelastic attenuation. *Journal of*
1121   *Geophysical Research: Solid Earth*, *117*(6), 1–20. https://doi.org/10.1029/2012JB009208

1122   Lin, P.-Y. P., Gaherty, J. B., Jin, G., Collins, J. A., Lizarralde, D., Evans, R. L., & Hirth, G.
1123   (2016). High-resolution seismic constraints on flow dynamics in the oceanic asthenosphere.
1124   *Nature*, *535*(7613), 1–9. https://doi.org/10.1038/nature18012

1125   Liu, H., Anderson, D. L., & Kanamori, H. (1976). Velocity dispersion due to anelasticity;
1126   implications for seismology and mantle composition. *Geophysical Journal of the Royal*
1127   *Astronomical Society*, *47*, 41–58. https://doi.org/10.1111/j.1365-246X.1976.tb01261.x

1128   Liu, Y., & Holt, W. E. (2015). Wave gradiometry and its link with Helmholtz equation solutions
1129   applied to USArray in the eastern U.S. *Journal of Geophysical Research: Solid Earth*, *120*,
1130   5717–5746. https://doi.org/10.1002/2015JB011982

1131   Ma, Z., Dalton, C. A., Russell, J. B., Gaherty, J. B., Hirth, G., & Forsyth, D. W. (2020). Shear
1132   attenuation and anelastic mechanisms in the central Pacific upper mantle. *Earth and*
1133   *Planetary Science Letters*, *536*, 116148. https://doi.org/10.1016/j.epsl.2020.116148

1134   Mark, H. F., Lizarralde, D., Collins, J. A., Miller, N. C., Hirth, G., Gaherty, J. B., & Evans, R. L.
1135   (2019). Azimuthal Seismic Anisotropy of 70-Ma Pacific-Plate Upper Mantle. *Journal of*
1136   *Geophysical Research: Solid Earth*, *124*, 1889–1909.
1137   https://doi.org/10.1029/2018JB016451

1138   Mark, H. F., Collins, J. A., Lizarralde, D., Hirth, G., Gaherty, J. B., Evans, R. L., & Behn, M. D.

(2021). Constraints on the Depth, Thickness, and Strength of the G Discontinuity in the Central Pacific From S Receiver Functions. *Journal of Geophysical Research: Solid Earth*, *126*, e2019JB019256. https://doi.org/10.1029/2019JB019256

McCarthy, C., & Takei, Y. (2011). Anelasticity and viscosity of partially molten rock analogue: Toward seismic detection of small quantities of melt. *Geophysical Research Letters*, *38*(18), 3–7. https://doi.org/10.1029/2011GL048776

McCarthy, C., Takei, Y., & Hiraga, T. (2011). Experimental study of attenuation and dispersion over a broad frequency range: 2. the universal scaling of polycrystalline materials. *Journal of Geophysical Research: Solid Earth*, *116*(9), 1–18. https://doi.org/10.1029/2011JB008384

Priestley, K., & McKenzie, D. (2013). The relationship between shear wave velocity, temperature, attenuation and viscosity in the shallow part of the mantle. *Earth and Planetary Science Letters*, *381*, 78–91. https://doi.org/10.1016/j.epsl.2013.08.022

Richards, F. D., Hoggard, M. J., White, N., & Ghelichkhan, S. (2020). Quantifying the Relationship Between Short-Wavelength Dynamic Topography and Thermomechanical Structure of the Upper Mantle Using Calibrated Parameterization of Anelasticity. *Journal of Geophysical Research: Solid Earth*, *125*(9). https://doi.org/10.1029/2019JB019062

Ruan, Y., Forsyth, D. W., & Bell, S. W. (2018). Shear attenuation beneath the Juan de Fuca plate: Implications for mantle flow and dehydration. *Earth and Planetary Science Letters*, *496*, 189–197. https://doi.org/10.1016/j.epsl.2018.05.035

Russell, J. B., & Gaherty, J. B. (2021). Lithosphere Structure and Seismic Anisotropy Offshore Eastern North America: Implications for Continental Breakup and Ultra-Slow Spreading Dynamics. *Journal of Geophysical Research: Solid Earth*, *126*, e2021JB022955. https://doi.org/10.1029/2021JB022955

Russell, J. B., Gaherty, J. B., Lin, P.-Y. P., Lizarralde, D., Collins, J. A., Hirth, G., & Evans, R. L. (2019). High-Resolution Constraints on Pacific Upper Mantle Petrofabric Inferred From Surface-Wave Anisotropy. *Journal of Geophysical Research: Solid Earth*, *124*(1). https://doi.org/10.1029/2018JB016598

Saikia, U., Rychert, C. A., Harmon, N., & Michael Kendall, J. (2021). Seismic Attenuation at the Equatorial Mid-Atlantic Ridge Constrained by Local Rayleigh Wave Analysis From the PI-LAB Experiment. *Geochemistry, Geophysics, Geosystems*, *22*, 1–16. https://doi.org/10.1029/2021GC010085

Sarafian, E., Evans, R. L., Collins, J. a, Elsenbeck, J., Gaetani, G. a, Gaherty, J. B., et al. (2015). The electrical structure of the central Pacific upper mantle constrained by the NoMelt experiment. *G3*, *16*, 1115–1132. https://doi.org/10.1002/2014GC005709.Received

Schardong, L., Ferreira, A. M. G., Berbellini, A., & Sturgeon, W. (2019). The anatomy of uppermost mantle shear-wave speed anomalies in the western U.S. from surface-wave amplification. *Earth and Planetary Science Letters*, *528*, 115822. https://doi.org/10.1016/j.epsl.2019.115822

Seton, M., Müller, R. D., Zahirovic, S., Williams, S., Wright, N. M., Cannon, J., et al. (2020). A Global Data Set of Present-Day Oceanic Crustal Age and Seafloor Spreading Parameters. *Geochemistry, Geophysics, Geosystems*, *21*, e2020GC009214. https://doi.org/10.1029/2020GC009214

1181   Takei, Y. (2002). Effect of pore geometry on Vp/Vs: From equilibrium geometry to crack.
1182   *Journal of Geophysical Research*, *107*(B2), 2043. https://doi.org/10.1029/2001jb000522

1183   Tromp, J., & Dahlen, F. A. (1992). Variational Principles For Surface Wave Propagation On A
1184   Laterally Heterogeneous Earth-Iii. Potential Representation. *Geophysical Journal*
1185   *International*, *112*, 195–209. https://doi.org/10.1111/j.1365-246X.1993.tb01449.x

1186   Webb, S. C., & Crawford, W. C. (1999). Long-period seafloor seismology and deformation
1187   under ocean waves. *Bulletin of the Seismological Society of America*, *89*(6), 1535–1542.
1188   https://doi.org/10.1785/bssa0890061535

1189   Yamauchi, H., & Takei, Y. (2016). Polycrystal anelasticity at near-solidus temperatures. *Journal*
1190   *of Geophysical Research: Solid Earth*, *121*, 7790–7820.
1191   https://doi.org/10.1002/2016JB013316

1192   Yang, Y., & Forsyth, D. W. (2006). Regional tomographic inversion of the amplitude and phase
1193   of Rayleigh waves with 2-D sensitivity kernels. *Geophysical Journal International*, *166*(3),
1194   1148–1160. https://doi.org/10.1111/j.1365-246x.2006.02972.x

1195